Analysis of the Monitoring Data of the Pierre Auger Surface Detector

MASTERARBEIT
zur Erlangung des akademischen Grades
Master of Science in Physics
(M.Sc.)

dem Fachbereich Physik der
Universität Siegen

vorgelegt von
Giovanni Fernando Alcocer Cordero

März 2008

Contents

Chapter 1

Introduction

1.1 Scope of the Thesis

The aim of this thesis is the monitoring and analysis of the data taking of the Pierre Auger Observatory (PAO), especially of the photomultipliers (PMTs) of the Surface Detector (SD). Monitoring data is used to study the evolution of some parameters of the PMTs. It provides an indicator of the PMT's performance. The results of the analysis are summarized according to the different patterns of the PMTs with the objective to select thresholds for the creation of the corresponding monitoring alarms.

- The chapter 1 contains an introduction to Cosmic Rays and the PAO.
- Chapter 2 is dedicated to describe the calibration system, the trigger system of the SD and the monitoring data.
- In chapter 3 the definitions of the observable parameters and examples of them are presented.
- In chapter 4 raining PMTs are analyzed.
- In chapter 5 the analysis of the another bad behaviour of the PMTs is presented.
- The alarms development is given in chapter 6.
- Finally the chapter 7 contains the summary and conclusions.

1.2 History of Cosmic Rays

Julius Elster and Hans Geitel noticed an unknown ionizing source in the air in their research of the atmospheric electricity. Independently, Charles Wilson suspected the existence of an ionization agent in his study with the ionization chamber. They reasoned that the ionization could be caused by an unknown radiation of large penetration, because even when the ionization chamber was shielded, they observed ionization. Wilson called it "cosmic radiation" because he supposed that the radiation might come from extraterrestrial sources.

In 1911, Victor Hess discovered the cosmic rays by using a balloon-borne pressurized ionization chamber [1]. Firstly, a slight diminution of ionization was observed by him while the balloon went up and after he detected a fast increase of ionizing radiation that persisted up to an altitude of 5 km. Later, Werner Kolhörster investigated this radiation with more refined techniques that confirmed the ionization up to an altitude of 9 km. So, the conclusion was that the ionization agent came from a high level and it was called "Höhenstrahlung". D. V. Skobeltzin observed tracks of charged particles by using a cloud chamber in his cosmic ray investigations. Also, Walter Bothe and Kolhörster identified charged particles by using Geiger-Müller counters.

Robert Millikan thought that the cosmic rays could be due to the spontaneous destruction of nuclei, such as carbon, nitrogen, and oxygen. On the other hand, Oscar Klein took into account the option that the matter and the antimatter forming galaxies and antigalaxies could annihilate to release an enormous amount of energy. In addition, Fred Hoyle assumed the possibility of the ejection of very heavy nuclei in supernova outbursts. Furthermore, Enrique Fermi proposed the statistical acceleration produced from collisions of charged particles with interstellar clouds.

In 1938, Pierre Auger noticed time coincidences in two surface detectors located many meters from each other and he observed showers with energies of around 10^{15} eV. So, Auger had discovered the "air shower", showers of secondary particles caused by the collision of primary high energy particles with molecules of the atmosphere.

In 1960, cosmic microwaves background (CMB) was discovered by Arno Penzias and Robert Wilson . Afterward, Kenneth Greisen, Vadem Kuzmin and Georgi Zatsepin concluded that cosmic rays of high energies would interact with the microwave background radiation. In this process, the energy of those high energy cosmic rays would be reduced and so that particles particles traveling a long distance could not have energies more than a threshold energy of a few times 10^{19} eV. It is known as the GZK (Greisen-Zatsepin-Kuzmin) cutoff.

But in 1991, the Fly's Eye cosmic ray team in the U.S detected a cosmic ray with an energy of 10^{20} eV. In 1994, also an event with energy of around 10^{20} eV was reported in Japan in the AGASA experiment [2]. In order to analyze those high energy cosmic rays with more statistics the Pierre Auger Observatory in Malargue, Argentina was designed in 1995. The origin and the evolution of the Universe could be understood by tracing high energy cosmic rays to their unknown sources.

1.3 Air Showers

It is possible to distinguish between primary cosmic rays and secondary cosmic rays. Primary cosmic rays are incident at the top of the atmosphere and the secondary cosmic rays are produced by the primary rays in the propagation through the atmosphere. Primary particles consist mainly of proton (86%), α particles (11 %), nuclei of heavier elements up to uranium (1 %) and electrons or positrons (2 %) [3]. The secondary particles originate from the collision of the primary particle against the nuclei in the atmospheric air. In each interaction, part of the energy of the primary particle is lost in the production of secondary hadrons (principally pions) [4] [6]. The secondary particles can decay or interact again with an atom of our atmosphere and so on, inducing a cascade process of particles called Extensive Air Shower (EAS). The reaction products of an EAS can be detected with giant detectors on the Earth surface.

EAS are composed of the following components: hadronic component (nucleon component), electromagnetic, muonic and neutrino components (see Figure 1.1). The primary interaction is hadronic and occurs at an altitude of approximately 20 km above sea level [4]. All particles produced in an EAS are called cosmic radiation.
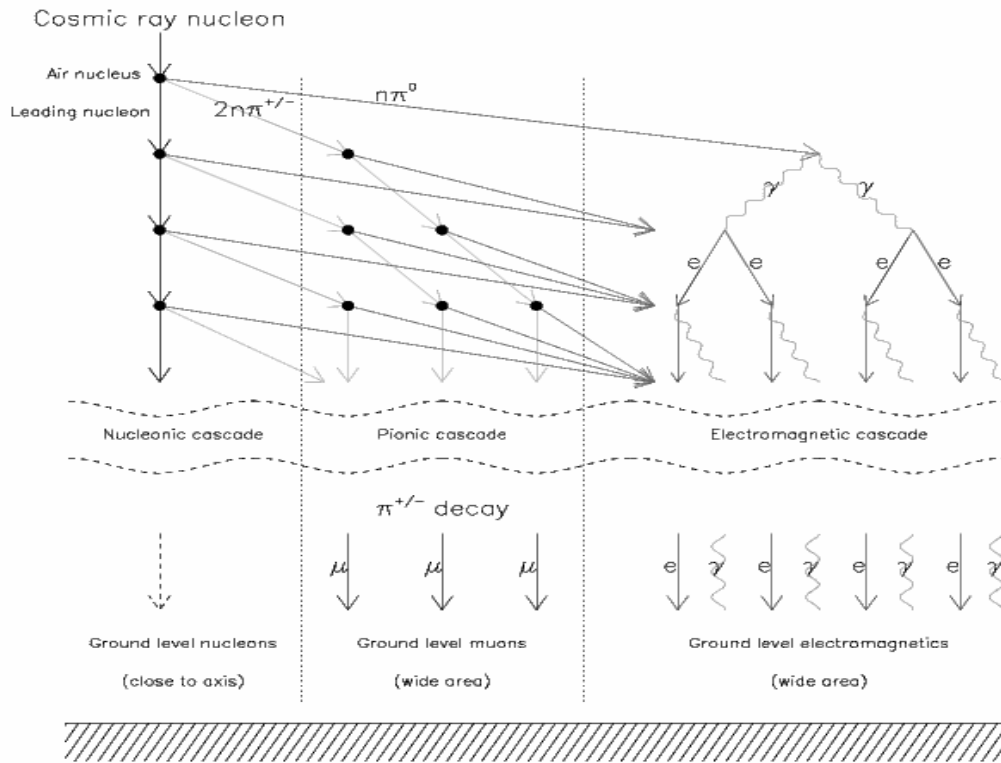
Figure 1.1: Schematic showing the developing of an EAS in the atmosphere [13].

The hadronic process can be described by the reaction:

$$N + N_{air} \longrightarrow N' + N'_{air} + \pi^o(\pi^\pm, K^o, K^\pm, n, p, ...) \quad ,$$
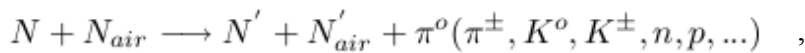
where N is the primary or secondary particle of the cosmic radiation and N_{air} is a nucleus of the atmosphere. The pions constitute most of the secondary particles of the hadronic component (around of 65 %) [5].

Some of the particles produced in the hadronic interactions are neutral pions, which mostly decay into two photons:

$$\pi^0 \longrightarrow \gamma + \gamma \quad .$$

7
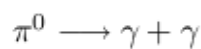
These photons initiate the electromagnetic cascade formed of photons, electrons and positrons. At each hadronic interaction, about 30 % of the hadronic component is transferred to the electromagnetic component [5]. Because the hadrons do many interactions, the most part of the initial energy is given to the electromagnetic component of the shower. I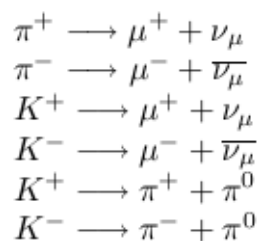n the electromagnetic component numerous photons, electrons and positrons are produced by Bremsstrahlung and pair production processes. Thus, photons, electrons and positrons are the most numerous particles in the evolution of the shower (around 99 % and carring about 85 % of the shower energy) [5]. Electrons, positrons and photons are absorbed rapidly (soft component) by interaction processes of them with the atmosphere and it causes that the electromagnetic component vanishes [4].

Other particles generated in the development of the air shower, are the charged mesons. The dominant ways of decay of their:

$$\pi^+ \longrightarrow \mu^+ + \nu_\mu$$
$$\pi^- \longrightarrow \mu^- + \overline{\nu_\mu}$$
$$K^+ \longrightarrow \mu^+ + \nu_\mu$$
$$K^- \longrightarrow \mu^- + \overline{\nu_\mu}$$
$$K^+ \longrightarrow \pi^+ + \pi^0$$
$$K^- \longrightarrow \pi^- + \pi^0$$

The muons form the muonic component and they decay with a lifetime of 2,2 * 10^{-6} . Due to their highly relativistic velocity, many of them reach the earth surface. The number of muons in the evolution of the shower is around 1% [5]. Muons are sufficiently energetic (hard component), rarely interact and only decay under weak interactions . It cause that they can reach the sea level and penetrate deep underground. Therefore, about 80 % of the charged particles at sea level are muons [4].

In the cascade process, muons and pions decays generate neutrinos and they constitute the neutrino component. Finally, the hadrons that survive the interactions contribute to the hadronic component [5].

1.4 Energy Spectrum of the Cosmic Rays

The energy spectrum of primary cosmic rays can be described as a inverse power law:

$$\frac{dF}{dE} \propto E^{-\gamma} \quad (1.1),$$

where F is the flux of the cosmic rays, E is the energy of them and γ is the spectral index.

Figure 1.2 shows a plot of the flux of cosmic rays versus their energy. The spectrum can be divided into three regions well-known with the names of knee (two first regions) and ankle (third region). The first knee appears around $3 * 10^{15}$ eV where the spectral index is between 2.7 and 3.0 [5]. The second knee is located at around 10^{17} and 10^{18} eV where the spectral index is between 3.0 and 3.3. The ankle is in the region of $3 * 10^{18}$ eV. Above this energy the spectrum is more concave with a spectral index of 2.7. For these energies the flux of the particles is less than 1 particle per km² per year.
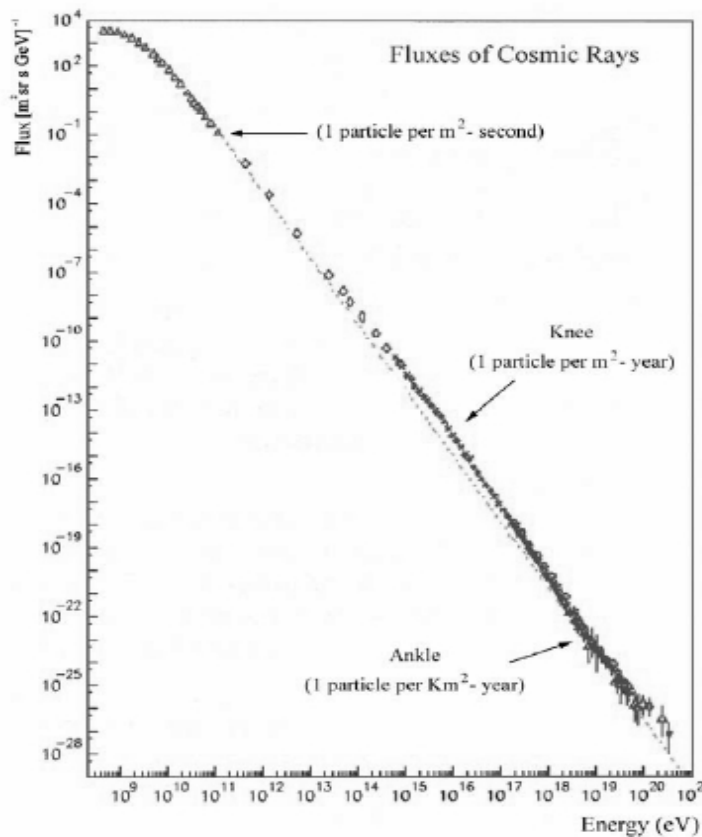

Figure 1.2: Fluxes of Cosmic Rays [14].

The origin of the cosmic rays for the first two regions of the energy spectrum is in our galaxy and their energies can be explained by the acceleration mechanism of Fermi. For the third region, there are many open questions like origin of cosmic rays, primary composition and acceleration mechanisms.

1.5 Ultra-High Energy Cosmic Rays

In 1930, Pierre Auger and his colleagues observed coincidences between two or more detectors separated by a distance of more than 300 m. They associated those coincidences with showers of cosmic rays (EAS) triggered by the arrival of a single cosmic ray of high energy at the top of the atmosphere [7] .

In 1991, Hungye Dai was analyzing the data from the Fly's Eye experiment in the Utah sky. The faint flashes of ultraviolet light produced in the sky when the cosmic ray particles hit the upper atmosphere was monitored and a very high energy event of $3*10^{20}$ eV was reported. Other experiments like the Akeno Giant Air Shower (AGASA) in Japan (1993-2004) announced other events with energies above 10^{20} eV [8].

In 1995, Cronin and Watson began to impel the PAO, an international effort that involves 15 countries: Argentina, Australia, Bolivia, Brasil, Czech Republic, France, Germany, Italy, Poland, Mexico, Slovenia, Spain, United Kingdom, USA and Vietnam [9]. They had the vision of two observatories, one in the Northern hemisphere and another one in the Southern hemisphere in order to cover the entire sky.

1.5.1 The GZK cutoff

A sharp cutoff at approximately several times 10^{19} eV in the energy spectrum of cosmic rays is expected due to energy degradation of the cosmic rays through their interaction with photons of the microwave background radiation. It is known as the GZK (Greisen-Zatsepin-Kuzmin) cutoff. Primary protons in this range of energies collide with photons of the microwave background radiation and enter in the region of resonances (unstable barions) via the equations:

$$\gamma + p \longrightarrow \Delta^+$$
$$\Delta^+ \longrightarrow p + \pi^0$$
$$\Delta^+ \longrightarrow n + \pi^+$$
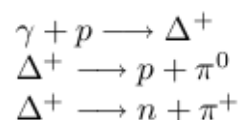
Appling four momentum conservation for the reaction:

$$\gamma + p \longrightarrow p + \pi^0$$

for a proton with mass M, momentum p, Energy E, pion of mass m, microwave photon with momentum q and energy qc (in order to simplify the initial formulations we use natural units, so c=1):

$$(E+q)^2 - (p+q)^2 = (M+m)^2 \qquad , \qquad (1.2)$$
$$M^2 + 2q(E - |p|cos\theta) = M^2 + m^2 + 2Mm \qquad . \qquad (1.3)$$

For a head-on collision θ=180° (most favorable case for the reaction) and so (1-cos θ)=2. Due to the fact that the proton is extremely relativistic, we have E=p and so the resulting equation for the threshold energy is:

$$E = m\frac{(M+\frac{m}{2})}{2q} \qquad . \qquad (1.4)$$

Returning to the initial units:

$$E = mc^2\frac{(M+\frac{m}{2})c^2}{2qc} \qquad , \qquad (1.5)$$

where: m=139,57 MeV/c², M=938,27 MeV/c², and qc is the energy of the photon.

In order to determine this energy, we calculate the peak energy of the photons of the CMB. Appling Wien's law and the Einstein equation for the energy of photons:

$$\lambda_{peak} = \frac{2.9*10^6}{T}[nm] \qquad , \qquad (1.6)$$

$$E_{peak} = \frac{hc}{\lambda_{peak}} \qquad . \qquad (1.7)$$

Replacing T=2,7 K (temperature of the microwave background) and hc=1240 [eV.nm], the typical CMB photon energy is around 1.16 meV.

Finally replacing this value in our equation of the threshold energy E (formula 1.5) we obtain:

Threshold energy: E≈6 * 10^{19} eV.

It is possible to do the calculations with the reaction for the barion obtaining exactly the same threshold energy. A nucleon with initial energy above 10^{20} eV loses about 1/5 of E_o (initial energy) in each interaction and the mean free path for collision is given by the formula:

$$\lambda = \frac{1}{\rho\sigma} \, , \qquad\qquad (1.8)$$

where σ is the cross section near the threshold energy for the interaction of high energy protons with photons of the microwave background radiation.
The values of σ and ρ where ρ is the microwave photon density are:
$\sigma = 2*10^{-28}$ cm²
$\rho = 400$ cm⁻³.
Replacing those values in (1.8) , we have $\lambda \approx 9.5$ Mpc (where 1 Mpc=1.31 * 10^{24} cm).
Applying the simple exponential model for the energy evolution of the shower:

$$E = E_o e^{-\varepsilon l} \, , \qquad (1.9)$$

where:
 l is the traveling distance of the nucleon,

 ε is a constant to be determined by replacing:

$E_o = 10^{20}$ eV ,
$E = 6*10^{19}$ eV (cuttof energy),

$l = 9.5 Mpc$.

 Thus the value of the constant is:
 $\varepsilon = 0.05$ Mpc⁻¹ .

And the resulting equation is:

$$E = E_o e^{-0.05 l} \qquad . \qquad (1.10)$$

This means that the energy of the nucleon is reduced by a factor of : $e^{-0.05 l}$.

Thus, a nucleon of initial energy of 10^{20} eV will have its energy reduced to 6 * 10^{19} eV (GZK cuttof energy) after traveling a distance of approximately 50 Mpc given by last formula.

For larger initial energy the cross section increases and leads to a similar maximal distance of less than 100 Mpc.

It is possible to conclude :

- A nucleon at Earth, which traveled a distance more than 100 Mpc, will have always an energy less than 10^{20} eV independent of the initial energy.
- Particles with an observed energies above 10^{20} eV are limitted to distances of approximately less than 100 Mpc from the Earth.

Nevertheless, the AGASA experiment showed a significant number of events with energies beyond the GZK cutoff and for this reason a giant air shower array, Pierre Auger Observatory, is built to study these very rare high energy cosmic rays. The energy spectrum of the AGASA experiment is shown in Figure 1.3 where it is possible to observe some events with energies more than 10^{20} eV.
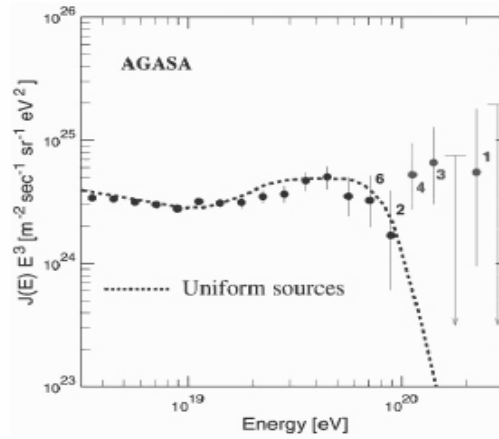

Figure 1.3: Energy spectrum from AGASA experiment (dots). The plot with the bars is the expected spectrum assuming the cosmological uniform distribution of the sources [2].

1.5.2 Deflection angle of high energy cosmic rays in the propagation through the galactic and extragalactic magnetic fields

In order to calculate the deflection of a charged cosmic ray in extragalactic and galactic magnetic fields, the derivation of the most simple formula is given below. The force due to the magnetic field B will act on the charged particle q via the equation:

$$F = qvB \quad , \qquad (1.11)$$

where B is the magnetic field directed away from us. The particles enter in the magnetic field with their velocities being perpendicular to the magnetic field lines.

13

So, the magnetic force acting on the particle is perpendicular to its movement (right hand rule).   Thus, the particle is forced to move on a circular path with radius r_B as it is shown in Figure 1.4.
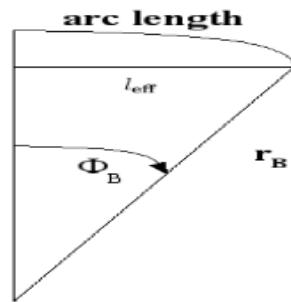

Figure 1.4: Deflection of the charged particle in the magnetic field.

This force is also equal to the centrifugal force:

$$F = \frac{mv^2}{r_B} \, , \qquad (1.12)$$

where m is the mass of the particle and r_B is the radius of the circular trajectory.

Equaling both equations (1.11 and 1.12) the resulting equation for the radius r_B is:

$$r_B = \frac{mv}{qB} \, , \qquad (1.13)$$

$$r_B = \frac{pc}{qcB} \, , \qquad (1.14)$$

$$. \; r_B = \frac{E}{qcB} \; . \qquad (1.15)$$

In order to bring the equation to astrophysic units, are used the conversions:

1 eV=1.6 * 10^{-19}J, 1T (Tesla)=10^4 Gauss, B_{ng}=(B/10^{-9}) , E_{20}=(E/10^{20}) .

So, the Larmor radius of a cosmic nucleus traveling in a magnetic field is given by the equation:

$$r_B \approx \frac{100 E_{20}}{Z B_{ng}} Mpc \quad , \qquad (1.16)$$

where Z is the atomic number of the particle.

For the angle deflection in the magnetic field (see figure 1.4), the equation is:

$$sin \Phi_B = \frac{l_{eff}}{r_B} \quad , \qquad (1.17)$$

where:

   l_{eff} is the path length (in units of Mpc).

So, replacing the Larmor radius in 1.17, is obtained the equation:

$$sin \Phi_B = \frac{l_{eff} Z B_{ng}}{100 E_{20}} \quad . \qquad (1.18)$$

Considering the aproximation for small angles: $\phi_B \ll 1$,

the resulting equation is:

$$\cdot \; \Phi_B \approx \frac{l_{eff} Z B_{ng}}{100 E_{20}} \quad . \qquad (1.19)$$

So, it is important to consider the thresholds values of the path length and the galactic and the extragalactic magnetic fields in order to have the maximum and the minimum angles. They are given in the next table1.1.

Values of the Galactic magnetic field: 10^{-8} G < B < 10^{-6} G

Values of the extragalactic magnetic field: 10^{-12} G < B < 10^{-9} G

Distances to galactic sources: l_{eff} <30kpc

Distances to extragalactic sources: l_{eff} >30 Mpc

Table 1.1: Threholds values for the magnetic fields and distances to the sources [10], [11] , [12].

We consider E = 1 * 10^{20} eV and two cases of particles: a proton (Z=1) and Iron (Z=13, product of stellar evolution). We use the threshold of the path length (30 Mpc) and the both limits of the extragalactic magnetic field. Thus, we can obtain the next table 1.2.

For B=1*10^{-12} G, l_{eff} =30 Mpc

E	Z	$\Phi_B(^o)$
1*10^{20} eV	1	3*10^{-4}
1*10^{20} eV	13	3,9*10^{-3}

For B=1*10^{-9} G, l_{eff} =30 Mpc

E	Z	$\Phi_B(^o)$
1*10^{20} eV	1	0,3
1*10^{20} eV	13	3,9

Table 1.2: Deflection angle, of cosmic rays which travel through the extragalactic magnetic field.

For the galactic magnetic field, we use the threshold of the path length (0,030 Mpc) and the both limits of the galactic magnetic field. So, we can obtain the next table 1.3.

For B=1*10^{-8} G, l_{eff} =0,030 Mpc

E	Z	$\Phi_B(^o)$
1*10^{20} eV	1	3*10^{-3}
1*10^{20} eV	13	3,9*10^{-2}

For B$_{ng}$=1*10^{-6} G, l_{eff} =0,030 Mpc

E	Z	$\Phi_B(^o)$
1*10^{20} eV	1	0,3
1*10^{20} eV	13	3,9

Table 1.3: Deflection angle of cosmic rays which travel through the galactic magnetic field.

Also, if we consider the special case of the galactic center:

l_{eff} = 8,5 kpc, with B=1*10^{-7} G, E=1*10^{19} eV and Z=13 (iron) the deflection angle is 1.1°.

For Z=1 (proton) it is 0.08°. It is possible to observe from the tables that the deflection angles are very small for considered cases, thus UHECR arrival directions should point back to their sources in the sky. So, an experiment able to provide data with high quality and statistical significance in the upper-end of the cosmic ray spectrum, good angular resolution and the uniform exposure over the whole sky is necessary. With these objectives in mind the Pierre Auger Observatory was built.

1.6 The Pierre Auger Observatory (PAO)

The main objectives of the PAO are to understand the nature, origin and the propagation of UHECR. The PAO is designed for complete-sky coverage with an aperture of at least 7350 km^{2}sr in each hemisphere in order to detect events with energies above 10^{19} eV. The southern observatory campus is located in Malargue, Argentina [9].

The PAO is measuring energy, arrival direction and mass composition of cosmic rays with very high statistical precision with two sub-systems: a Surface Detector (SD) and a Fluorescence Detector (FD).   The array of surface detectors measures the lateral and temporal distribution of shower particles at ground level.

The Surface Detector of the PAO is composed of 1600 water Cherenkov detectors arranged in a hexagonal grid with 1.5 km spacing between detectors. They cover a total area of 3000 km^2. The layout is shown in Figure 1.5.
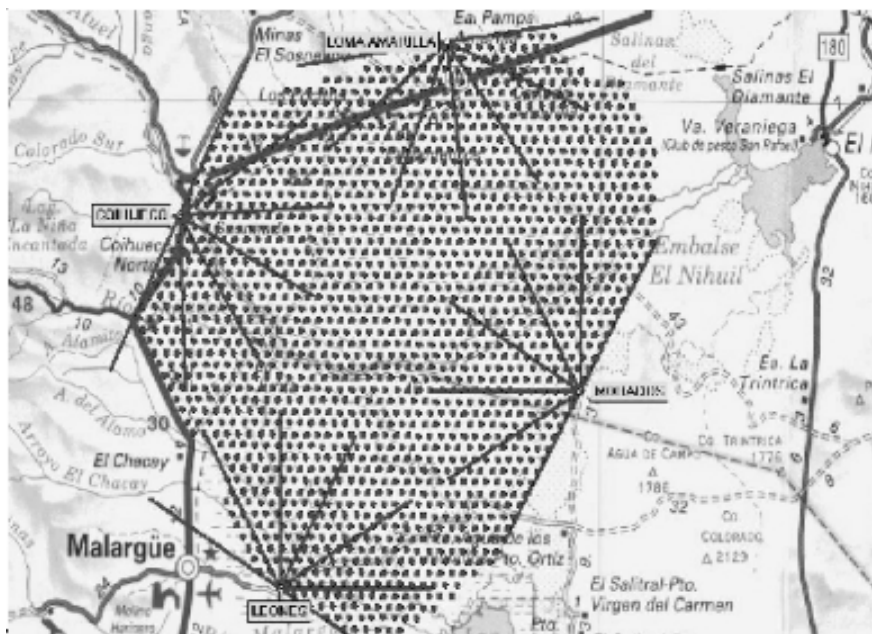
Figure 1.5: Layout of the Pierre Auger Observatory (dots are the SD tanks) [16].
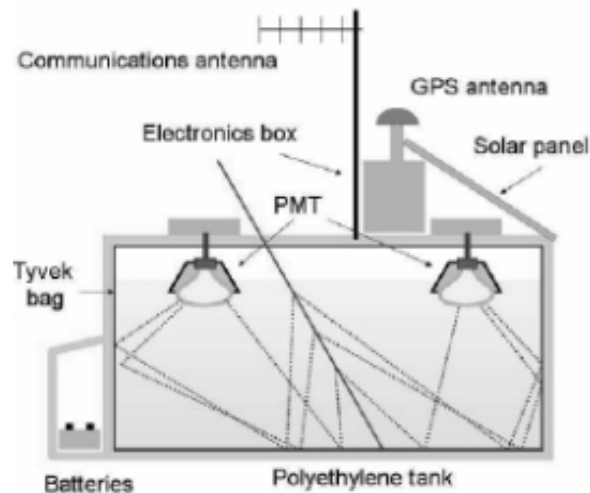
A water Cherenkov detector is shown in Figure 1.6.

Figure 1.6: Schematic view of a water Cherenkov tank [15]

Each detector station is a cylindrical tank with a surface of 10 m^2 and a height of 1.2 m, filled with 1200 litres of purified water [2].   Three photomultipliers collect the Cherenkov light emitted by charged particles in the EAS as they cross the tank.   These stations operate on battery-backed solar power and   communicate with a central station (central data acquisition system: CDAS) by using radio links. Event timing is provided through Global Positioning System (GPS) receivers.

The Fluorescence Detector of the PAO is composed of 4 stations located at: Loma Amarilla, Coihueco, Morados and Leones (see figure 1.5), each station having 6 telescopes. The 24 fluorescence telescopes are overlooking the array. They measure the longitudinal development of the shower in the atmosphere. In the mirror focus of each telescope 440 phototubes are installed as a camera. The 4 stations measure the emission from atmospheric nitrogen which is excited by the charged particles of the shower as they traverse the atmosphere and emit fluorescence light.

The PAO has been designed to work in a hybrid detection mode. Figure 1.7 shows the design of the hybrid detection of an air shower.
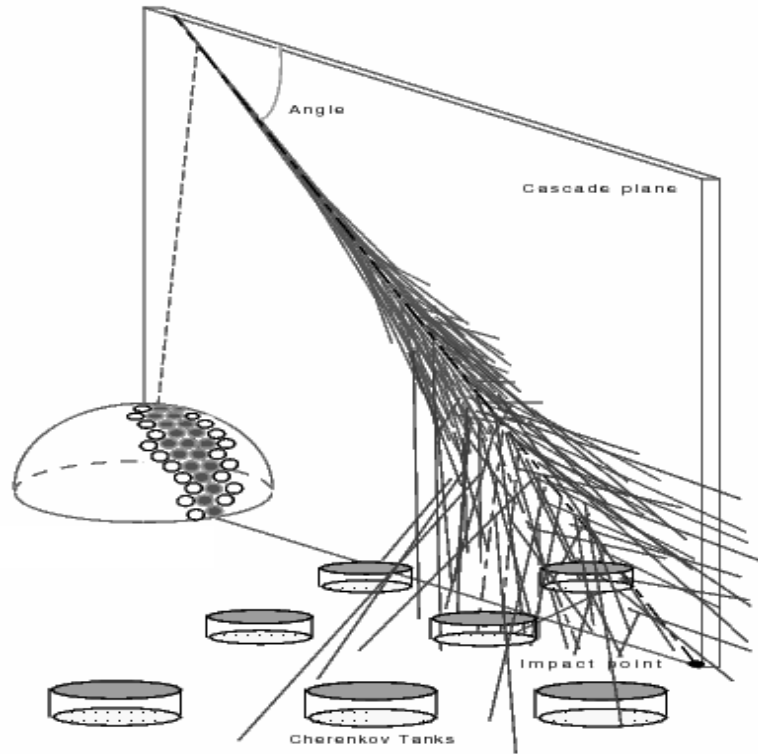
Figure 1.7: Schematic view of an air shower measured by both SD and FD. Black circles indicate the fired phototubes and the large cylinders are the water Cherenkov tanks [17].

       This hybrid technique will allow to measure the energy and arrival direction with high precision as well as very good separation of protons and heavy nucleis. The energy resolution for the hybrid technique is around 10 % at 10^{20} eV and the angular resolution is approximately 0.5° [2] . If the detection is performed only with the surface array the energy resolution is between 10% and 20 % and the angular resolution varies from 1° and 2°.

Chapter 2

Surface Detector Station and the Monitoring Data

2.1 Photomultiplier Signal

The secondary cosmic rays are observed by the emission of Cherenkov light as they traverse the water of a Surface Detector tank. The cherenkov light in one detector station is detected by 3 photomultiplier tubes (PMTs). The signal for an event of a cosmic ray air shower is mainly generated by electrons and muons in the shower. Other types of particles are insignificant. The energy of the electrons is lower than that of the muons and they cause smaller signals. The signal of a single muon recorded by a PMT in one SD tank is shown in Figure 2.1. The typical rise time of a muon signal is 10 ns with a decay time of around 70 ns. Figure 2.1 shows the single vertical muon signal recorded by a PMT of the surface station as it is observed with an oscilloscope.
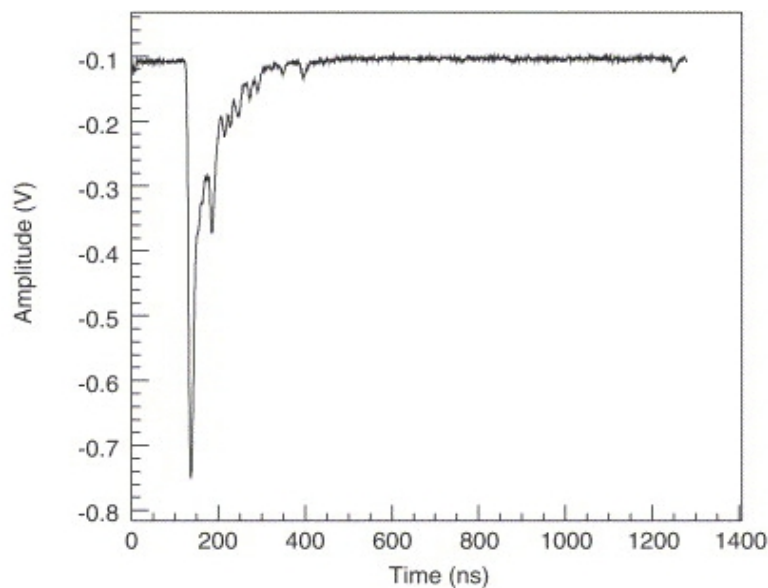
Figure 2.1: Single muon signal recorded by a PMT of a water cherenkov tank [18]

21

From each PMT of one station, the signal from the anode and from the last dynode are sent to the local station acquisition system (The Front-End board with 3 low-gain channels (anode) and 3 high-gain channels (last dynode)). The signal of the last dynode is inverted and amplified to an amount of 32 times to match the dynamic range. The signals are digitized every 25 ns with the support of 10-bit FADCs (Fast Analog Digital Converters) running at 40 Hz. The signals recorded from the FADC have units of ADC counts with a range of 0-1023, which correspond to an input range of 0-2 V. The signals recorded from the FADCs of one PMT (anode: left , dynode: right) is shown in Figure 2.2.
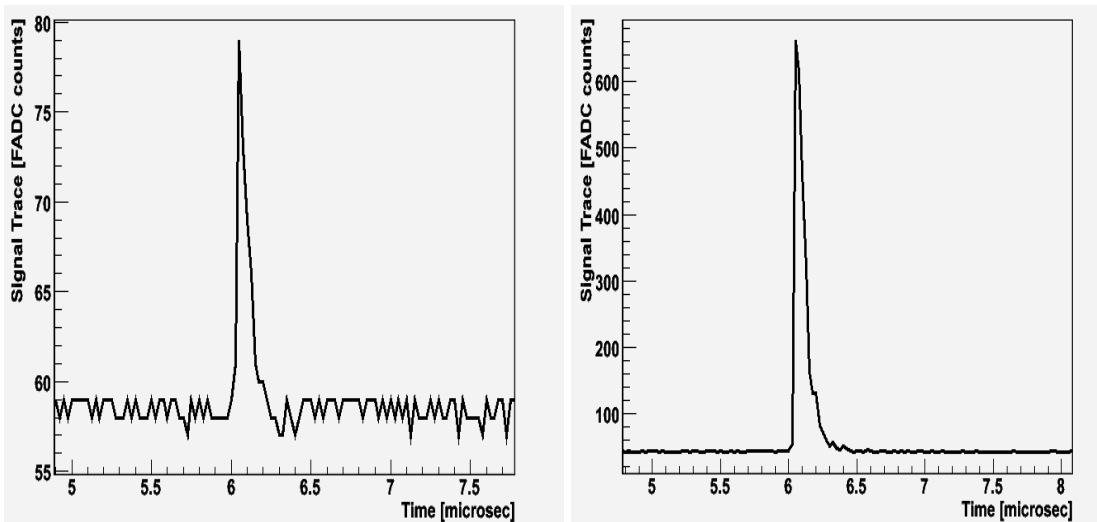
Figure 2.2: ADC traces recorded (anode: left, dynode: right) from the FADC of one of the PMT of the surface detector (LsId=201, PMT3) .

A single vertical muon generates a peak signal of approximately 30 photoelectrons per PMT in the interval of 25 ns. Nevertheless, for a shower of 10^{21} eV, the signal has around 20000 photoelectrons per PMT at a distance of 500 m from the shower axis [19]. It is necessary to have enough dynamic range for the signal in order to cover with very good precision the particle flux near the (around 100 particles μs^{-1}) and far away from the (approximately 1 particle μs^{-1}) shower core. Thus two channels, one with low gain and one with high gain, are used for each PMT. In order to have good calibration for both channels, a 5 bit overlop for both channels has been chosen. Afterwards, the ADC outputs are forwarded to the trigger system .

2.2 Surface Detector Calibration

Calibration of the SD is based on the average signal deposited in the tank by a single high energy muon traversing a tank vertically. This signal is called the vertical equivalent muon (VEM). The aim of the calibration procedure is to convert the ADC signal of the PMTs into VEM units and to obtain a uniform trigger for the surface detector.

In order to have reference values for the calibration, firstly measurements of the photocurrent and the charge deposited in a reference tank by a single vertical and central muon were done. Atmospheric muons passing through the detector give an excellent method to measure the value of 1 VEM, because they produce a peak in a pulse height histogram (I^{peak}_{VEM}) . I^{peak}_{VEM} is defined as the peak photocurrent produced by a vertical through going muon and corresponds around about 50 ADC counts for each PMT in the low gain channel [23] . This value was measured by using an external muon telescope from external triggers and by comparison with the measurements from the internal station trigger [31]. The muon telescope uses two scintillators, placed on the top and botton of one reference detector tank situated at the central campus..

The pulse height histogram for one PMT is shown in Figure 2.3 where the peak at around 50 ADC counts is due to single muon crossing the tank.

.
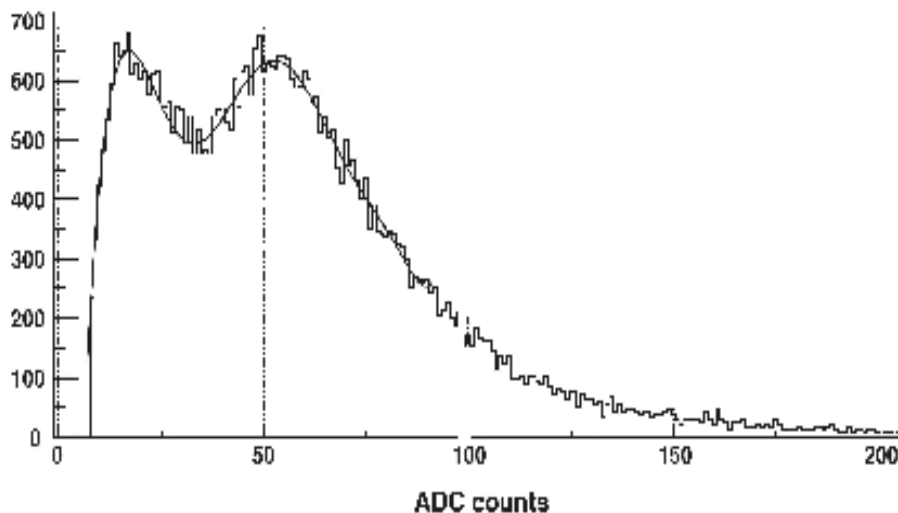
Figure 2.3: Pulse height histogram of a single PMT of reference tank [24].

This peak I^{peak}_{VEM} is related to the average charge deposited by a vertical and central through going muon, because the charge is the integrated signal of the current. So, the atmospheric muons also produce a peak (Q^{peak}_{VEM}) in a charge histogram. Therefore, I^{peak}_{VEM} is the peak in a pulse height histogram and Q^{peak}_{VEM} is the peak in a charge histogram. The peak Q^{peak}_{VEM} is at around 1.09 VEM summed over all 3 PMTs and (1.03±0.02) VEM for each PMT. This was measured in a special measurement with a muon telescope in a reference tank [20].

Figure 2.4 shows the peak Q^{peak}_{VEM} in a charge distribution for one PMT measured by using a muon telescope.

```
10³
10²
10
1
   0   0.5   1   1.5   2   2.5   3   3.5   4  VEM
```
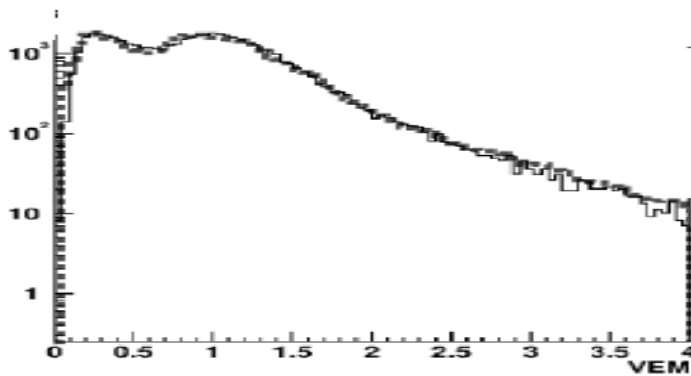
Figure 2.4: Charge histogram for one PMT of the reference tank in units of VEM (the peak is approximately at 1.03 VEM) [22].

The calibration of the Surface Detector is based on an procedure in three steps:
1) Set up the gains of each PMT at I^{peak}_{VEM} =50 ADC counts, by adjusting the high voltage of each PMT in order to have the trigger rates above a common threshold for the three PMTs using as reference unit for the threshold trigger the I^{peak}_{VEM}.
2) The development of the gains is monitored (local calibration) in order to adjust the level triggers and compensates drifts of the step 1.
3) The I^{peak}_{VEM} is stabilized by the step 2, the trigger is enabled and a set of charge and pulse height histograms are produced and sent to the central data acquisition system. The histograms have about 150000 per minute. Finally, we use the conversion factor from Q^{peak}_{VEM} to VEM (1.03±0.02) in order to have the conversion from the average of all samples to VEM units [23], [31].

In Figure 2.5, we can see examples of the charge integrated signal (charge histogram) and the amplitude signal (pulse height histogram) from a SD triggered by a 3-fold coincidence between all 3 PMTs with all PMTs summed. The dashed lines in the histogram are provided using an external muon telescope to select only the VEM.
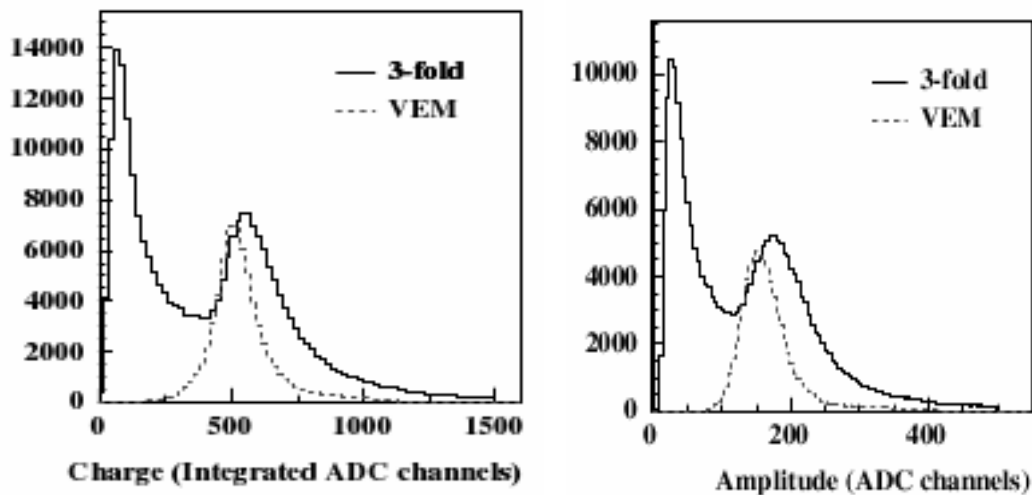

Figure 2.5: Charge histogram (left side) and Pulse height histogram (right side) from a SD station, triggered by a 3-fold coincidence between all 3 PMTs with the signal from all 3 PMTs summed (dashed histogram is measured using an external muon telescope to have only the VEM signal) [20].

The histograms are understood as the convolution of three diverse classes of next incoming particles :
(1) muons which enter through the top and exit through the botton (VEM) (second peak).
(2) muons which enter through the top or bottom and exit through the side (first peak).
(3) muons which enter through the side and exit through the side (first peak).
The first peak is due to the contribution of the second and third classes together with the spreading of the signal due to low energy particles. The second peak is due to vertical throughgoing atmospheric muons.

The histogram of the number of photoelectrons from a vertical muon for a single PMT is also shown in Figure 2.6.
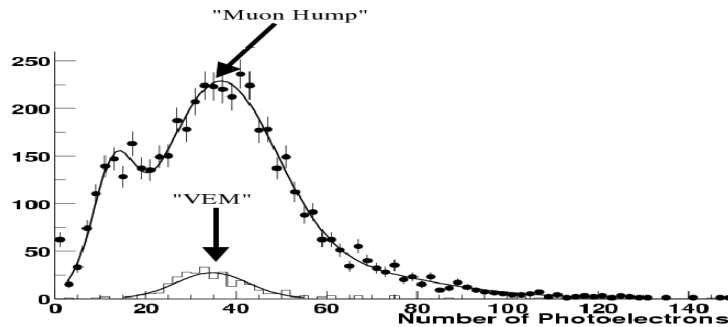
Figure 2.6: Charge distribution (number of photoelectrons) for a single PMT resulting from vertical muons crossing through the tank (solid line histogram) using muon trigger scintillators placed on the top and botton of the reference tank, and from the "internal trigger", simply requiring three fold coincidences of the three PMTs in a tank [21].

It is possible to observe in Figure 2.6 that the peak (1 VEM) corresponds to approximately 30 photoelectrons.

2.3 Trigger System

The trigger system of the surface station is hierarchic being composed of more trigger levels with local triggers in levels 1 (T1) and 2 (T2). The level 3 (T3) is formed at the Central Data Acquisition System (CDAS) based on the spatial and temporary correlation of the trigger level T2. All the data that satisfy T3 trigger will be stored. Additional level of triggers are used offline to select physical events (T4) and accurate events (T5).

I^{peak}_{VEM} is the common reference unit for the threshold of the triggers. The first trigger level T1 is evaluated by the PLD (programmable logic device) board and is composed of two different trigger modes:

 – three-fold coincidence of a 1.75 I^{est}_{VEM} threshold on each PMTs and 2.5 I^{est}_{VEM} for one PMT. The I^{est}_{VEM} is the estimated current for a Vertical Equivalent Muon. This trigger is used to detect fast signals (muonic component).
 – Time Over Threshold (ToT): 13 bins within a window of 120 bins above a threshold of 0.2 I^{est}_{VEM} in coincidence for two PMTs. It has a low rate of 1.6 Hz which corresponds to the expected rate of double muons for an Auger Surface Detector. This trigger is used to detect small and spread signals[25].

A signal may satisfy both conditions and the priority is given by the ToT.

26

The triggers T2 are evaluated by the local station system (local electronics is controlled by a CPU board that has a Power PC running at 40 MHz) and select from the T1 signals those probables ones to have come from EAS.   All the ToT triggers are promoted to T2 and the T1 threshold trigger is checked again for 3-fold coincidence above 3,2 I^{est}_{VEM} threshold and promoted to T2 trigger. The rate of the T2 triggers is around 20 Hz.   All T2 triggers are sent to the CDAS in order to do the correlation check between tanks.

The T3 triggers are evaluated by the CDAS event builder. The T3 triggers check the correlation in time and space for all stations sending T2 triggers. The coincidence of 3 adjacent tanks (minimum compactness requirement: one tank have one of its nearest neighbors and one of its second nearest neighbors triggered) that have passed the ToT condition is required for the T3 trigger. The left side of the figure 2.8 shows a possible 3-fold configuration. It selects principally physical events and the 90% of the chosen events are showers.   Another T3 trigger in this level requires a 4-fold coincidence (moderate compactness requirement) with the condition that one tank with T2 trigger can be up to 6 km far from others within a reasonable time window. This trigger is necessary in order to detect horizontal showers.   The right side of the figure 2.7 shows an example of the 4-fold configuration.
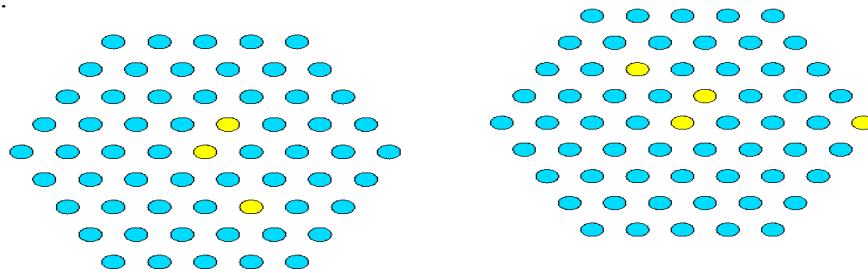
Figure 2.7: 3-fold and 4-fold coincidence for the T3 trigger level (triggered tanks: yellow color).

In order to select only showers from the T3 data, a physical trigger T4 is necessary. This physical trigger is used offline in order to select events with zenith angles below 60 degrees. Two behaviors of the vertical showers are used in order to do the selection: the 3 ToT compactness configuration of the triggered tanks or 4C1 compacity configuration (at least one fired station has 3 triggered tanks out of its 6 nearest neighbours).   Those configurations are show in the figure 2.8.
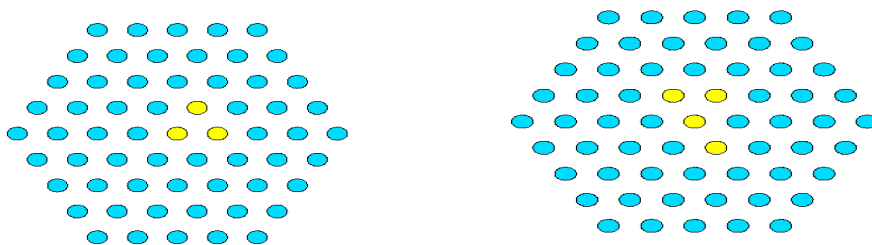

Figure 2.8: 3 ToT and 4C1 configurations for the T4 trigger level (triggered tanks: yellow color).

Between the events that pass the T4 trigger, only those events that can be reconstructed with a well-known energy and an angular precision will be used for the T5 quality trigger. It requires that the tank with the highest signal must have at least five active tanks among its 6 nearby neighbors and the reconstructed shower core must be within an equilateral triangle of active stations [25].

On the other hand, large fluctuations of ToT trigger rate produce an increase of the ToT trigger rate. It changes the threshold levels for the trigger system, affecting in this form the step 1 and 2 of the calibration procedure of surface detector. Because the conversion of the signal of the PMTs into VEM units (step 3) depends on the the step 2, so the fluctuations of the ToT trigger rate affects in this way to the calibration of the detector. In Figure 2.9 the left plot is the plot of the trigger efficiency versus the VEM signal and the right plot is the trigger efficiency versus the energy (for Iron, Proton, and Gamma rays).
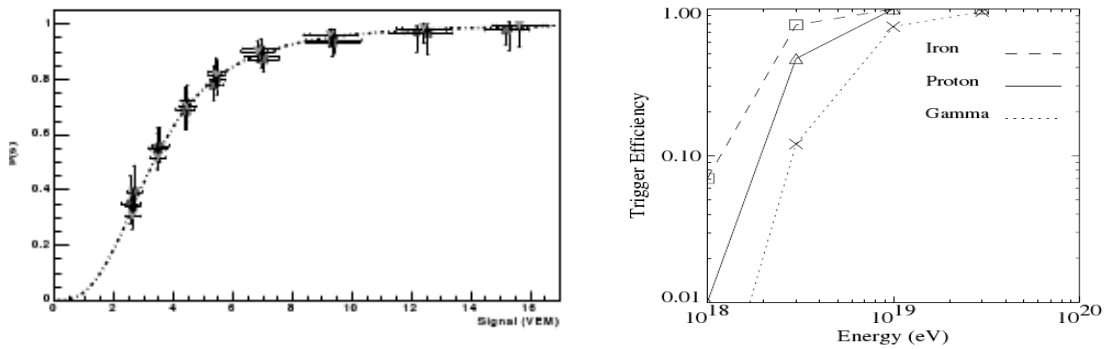
Figure 2.9: Probability for a local station to pass the trigger system in units of VEM and in units of eV (trigger efficiency). The right plot shows separatly the trigger efficiency for Iron, Proton and Gamma rays. [25] [27].

It is possible to observe in the figure 2.9 that for energies above 10^{19} eV, the trigger efficiency is 100 % saturated (VEM signal>>10 VEM, E>10^{19} eV) . Because the energy reconstruction is done in the region around of 10^{19} eV, trigger rate fluctuations does not affect it because the trigger efficiency is saturated [25].

2.4 Central Data Acquisition System (CDAS)

The Central Data Acquisition System (CDAS) was designed to assemble the triggers of the SD, to form the third level trigger of the detector, to allow the control of these detectors and to organize the storage of data. The data that are sent by the LS to CDAS correspond to some sections (streams):

- Trigger stream : mainly composed of the local trigger of the SD
- Control and Service Stream : it concerns the control of the configuration of the LS from the CDAS and also to download and test local station software.
- Data Stream : FADC traces and the information of the calibration are sent to CDAS when a event T3 has been identified.
- **Calibration and monitoring** : The LS is sending information of the monitoring and calibration. The calibration is performed every minute and sent to CDAS every 7 minutes for monitoring. [26].

2.5 Monitoring Data

In order to check the long term performance of the system and the accuracy of the online calibration, every 400 seconds (aproximately 7 minutes) monitoring data are recorded from each surface station to ensure that they are performing as intended and also to understand the detector behaviour. The monitoring data are averaged over 20 readings made every 20 seconds.

They are used to study the evolution of some parameters of the PMTs such as VEM Peak, VEM Area, VEM Area/Peak, Dynode signal, Anode signal, Dynode/Anode Ratio, ToT trigger rate as a function of both time and temperature. The Monitoring Data is structured as allows: data for short term contained in the table MonitCalib and long term contained in the table LongTermMonitCalib.

The table of MonitCalib has data available every 7 minutes. For this analysis we used data taken from 6 to 13 of December 2007. The following variables containing relevant information for the performance of the PMTs are available:
Voltage, Temperature, VEM Area, VEM Peak, VEM Area/Peak, Anode, Dynode, Dynode/Anode Ratio, ToT trigger rate.

The table of LongTermMonitCalib has data available from many months. One set of data is recorded every hour. For our analysis we have data from 7 June to 5 December 2007. This table has the following relevant variables for the performance of the PMTs:
Voltage, Temperature, VEM Area, VEM Peak, Dynode/Anode ratio.

Chapter 3

Observable Parameters in Monitoring Data

The observable parameters of the PMTs that are present in the monitoring data and were used in the analysis of this chapter are: VEM Peak, VEM Area, VEM Area/Peak, Pedestal of the Anode, Pedestal of the Dynode, Dynode/Anode Ratio, ToT trigger rate, Voltage, Temperature. The chosen station for the analysis is the LsId=164, PMT3. The data shown here is from the short term Monitoring Calibration database. The data is available for eight days, but due to some interruptions (recalibrations or data transfer problems) during the first days, it is shown for the five last days but still all the data being available can be used for the analysis.

3.1 PMT Temperature.

At the base of each PMT the temperature is measured. This value is used to analyse the behavior of the parameters of the PMTs as a function of the temperature. The temperatures in Malargue are in the range from -20 ºC to 60 ºC approximately with a large sinosoidal variation between temperatures at day and night. In Figure 3.1 the pattern of the temperature signal for one PMT in December 2007 is shown. The variation of the temperature between day and night is clearly visible.
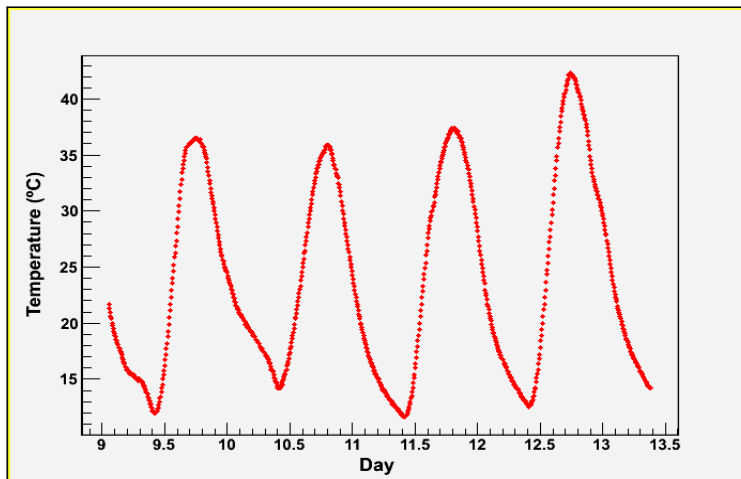
Figure 3.1: Plot of the Temperature of one PMT versus time.

3.2 VEM Peak

The VEM Peak is defined as the height of the signal of a vertical muon crossing the centre of the tank. A plot of a typical behavior for one PMT is given in Figure 3.2.
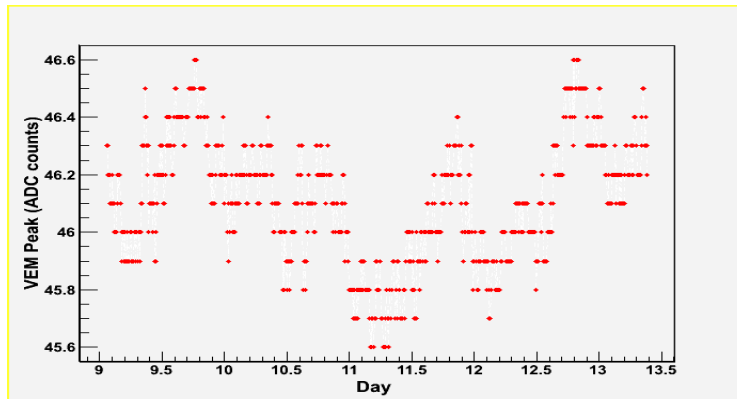
Figure 3.2: Plot of the VEM Peak versus time.

The average value is around 46 ADC counts with fluctuations in the order of 2 %. A small variations of the signal (around 1 ADC count) due to the temperature is observable in Figure 3.2.

3.3 VEM Area

The VEM Area is defined as the average area of a VEM signal. Therefore, the total charge deposited by a VEM signal is the VEM Area. In Figure 3.3, the general behaviour for one PMT is given.
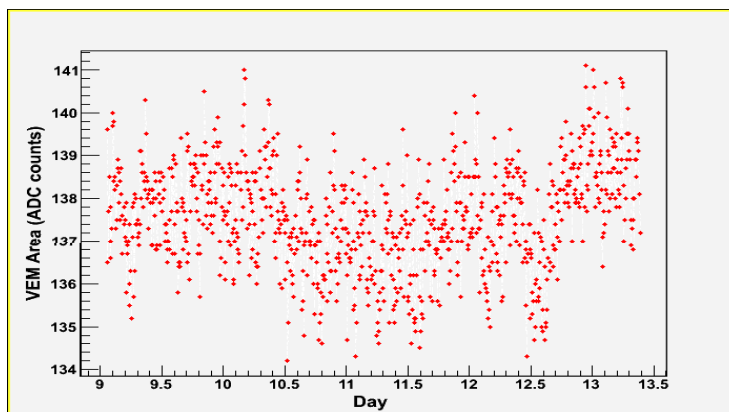
Figure 3.3: Plot of the VEM Area versus time.

The average value is around 138 ADC counts with fluctuations of around 2 %. In Figure 3.3 is possible to observe small variations in the order of 3 ADC counts, which is mainly due to temperature variations. The VEM Peak appears to be more sensitive to changes of the temperature than the VEM Area.

3.4 Ratio of VEM Area over VEM Peak

The VEM Area/Peak is a measure of the signal width. This ratio depends on the properties of the water and the Tyvek reflectivity of the tank. The behaviour of this variable is given in Figure 3.4.
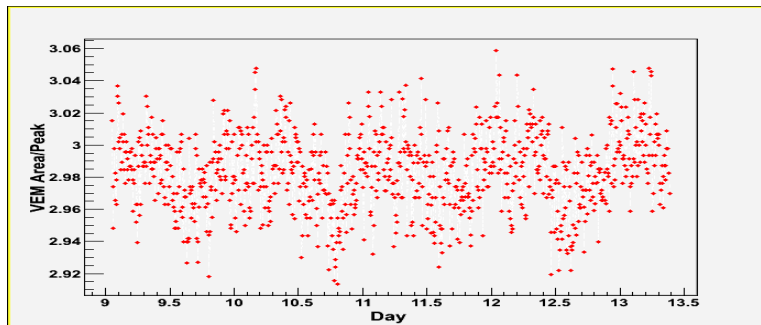
Figure 3.4: Plot of the VEM Area/Peak versus time.

The average of VEM Area/Peak is around 3 with fluctuations also of about 2 % .

3.5 Anode pedestal

The anode pedestal is the signal of the anode at the output of the amplifier when the PMT does not have an input signal. A typical plot of this variable for one PMT is given in Figure 3.5.
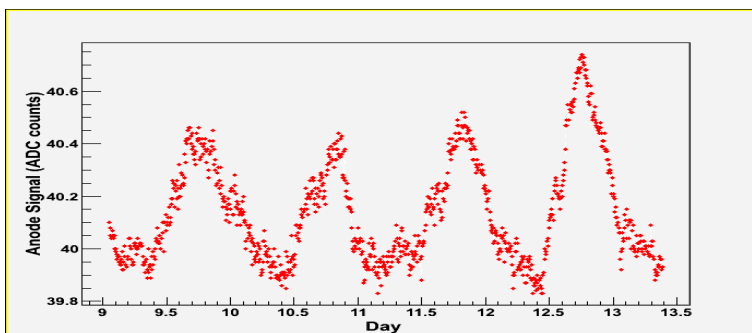
Figure 3.5: Plot of the Anode Pedestal versus time.

The average value for the anode pedestal is around 40 ADC counts and the fluctuations are around 1 %. It is possible to observe in the figure small variations of sinoidal form of around 1 ADC couns. If we compare this plot with Figure 3.1, we observe that there is a strong correlation with the temperature.

3.6 Dynode pedestal

The dynode pedestal is the signal of the last electrode before the anode at the output of the amplifier when the PMT does not have an input signal. The plot of this signal for one PMT is given in Figure 3.6. It shows the same behavior with the temperature as the anode pedestal, but the sinoidal variations are larger than the variations of the anode pedestal.
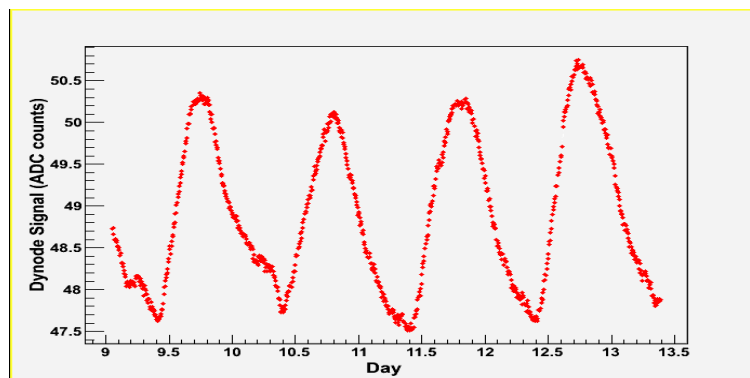
Figure 3.6: Plot of the Dynode Signal versus time.

The value for dynode pedestal is around 49 ADC counts with fluctuations of around 3 %. Also for this signal the strong linear correlation with the temperature is observed.

3.7 Dynode/Anode Ratio

The Dynode/Anode Ratio is defined as the ratio between the amplified signal (32 times) from the last Dynode stage to the signal at the Anode. This parameter is used in order to obtain the corresponding calibration of one VEM in the anode channel. For tanks close to the shower core, the dynode readout is saturated. For these events the signal measured on the anode should be used. Therefore, the accuracy of the signal size and the energy of the event depends of this parameter.

33

The typical pattern for one PMT is given in Figure 3.7.
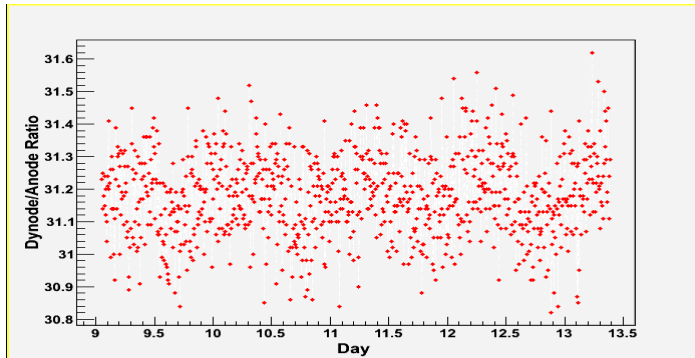
Figure 3.7: Plot of the Dynode/Anode Ratio versus time.

The average value for the signal of the Dynode/Anode is around 31 with fluctuations in the order of 2%.

3.8 ToT trigger rate

The ToT trigger rate importance comes from its capability to reduce the single muonic background significantly. So, to fulfill the ToT trigger the signal is required to be above a threshold , with a given coincidence between PMTs, for a minimum number of bins within a sliding window. The nominal ToT trigger rate condition needs that the signal has to be above 0.2 VEM in 2 PMTs for a minimum of 13 bins within a time window of 120 bins (chapter 2.2). The ToT trigger rate has a strong dependence on the water quality because as the quality of the water changes, the width of a muon signal and consequently the ToT trigger rate changes.

In Figure 3.8 the current behaviour of this parameter is shown. The typical value of the ToT trigger rate is 0.2-0.3 Hz.
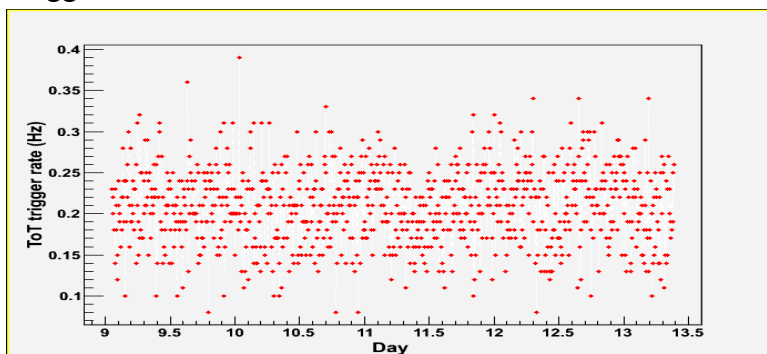
Figure 3.8: Plot of the ToT trigger rate versus time.

3.9 PMT High Voltage.

The high voltage of the PMT is the readout of the positive voltage applied to the PMT anode. This value should be stable with slight correlation with the temperature. Figure 3.9 shows a typical behaviour of this signal for one PMT.
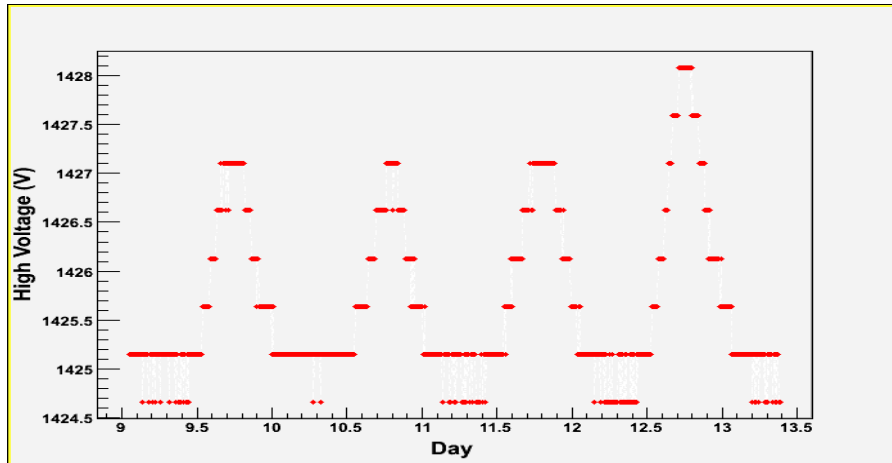
Figure 3.9: Plot of the High Voltage of the PMT versus time.

The High Voltage applied to the PMTs is in the range between 1000 and 1600 V. For some PMTs the High Voltage is changed in order to adjust (recalibration) the VEM value of the PMT. The High Voltage of the PMT is supplied by a battery of +12 V. Therefore, changes in the voltage of the battery also can affect the voltage output.

Chapter 4

Raining PMTs

4.1 Raining Behaviour

Some PMTs show abnormaly high fluctuations of the Vertical Equivalent Muon signal (VEM Peak) and the Dynode/Anode Ratio. They are called raining PMTs and the name is given for the raining pattern in the plot of these variables versus time. An example of a raining PMT compared to a normal PMT is shown in Figure 4.1.
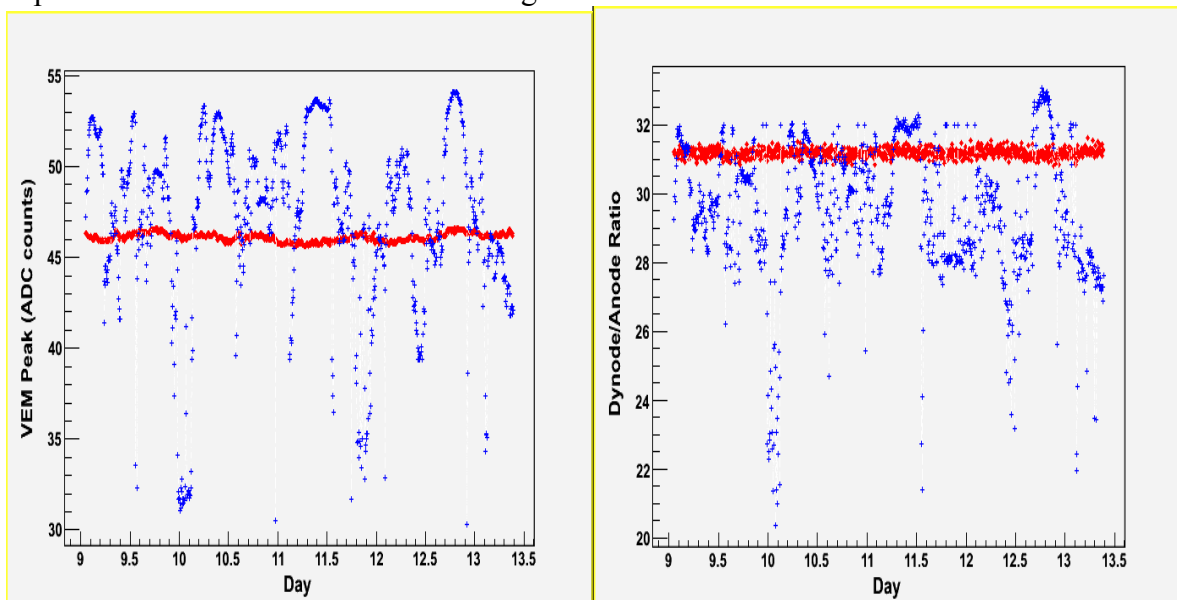
Figure 4.1: Plot of the VEM Peak and Dynode/Anode Ratio versus time (Good PMT, red color: LsId=164 PMT3; Raining PMT, blue color: LsId=818 PMT3).

So, for good PMTs the fluctuations are very small whereas for raining PMTs sudden fluctuations of often more than 10 ADC counts occur. The variations of the VEM Peak are correlated with the variations of the Dynode/Anode Ratio. The PMT instability seems to be caused by temperature variations and it is suspected that the reason is a bad ground connection on the PMT base [28]. They appeared firstly for stations deployed after January 2005 [29]. For this reason most of the stations with raining PMTs have Id>600.

The behaviour of the ToT trigger rate for a good (red color) and a raining PMT (blue color) is shown in the figure 4.2.
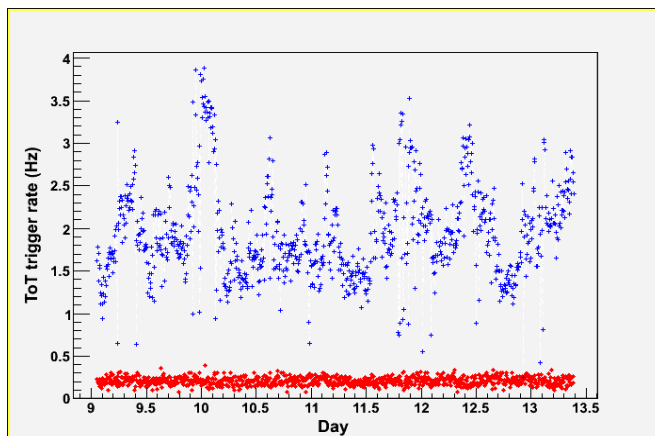
Figure 4.2: Plot of the ToT trigger rate versus time for the same chosen PMTs.

Thus, in Figure 4.2 it is possible to see that these fluctuations in the VEM Peak and Dynode/Anode Ratio induce an increase of the ToT trigger rate. It changes the threshold levels for the trigger system, affecting in this form the calibration of the detector (chapter 2.3, pag.24). The increase in the ToT trigger rate uses more bandwidth of the radio connection between the tanks and the central station. It also increases the chance probability for accidental coincidences.

4.2 Methods of the Analysis

In order to study the stability of the PMTs, the procedure of the analysis consists of selecting by eye:

- 100 good PMTs with stable values of the VEM Peak (low fluctuations).
- 100 raining PMTs with anomalous behaviour of the VEM Peak (large and abrupt fluctuations).

For both categories of PMTs the evolution of the RMS and the difference between the Maximum and Minimum for the parameters: Dynode/Anode Ratio, VEM Peak was studied as a function of time, station Id, voltage and temperature. The RMS and the Maximum-Minimum (MAX-MIN) are calculated from the monitoring data obtained during each day. The distributions of the VEM Peak and Dynode/Anode Ratio were also analysed. The analysis uses the data taken during 5 days between December 6th and 13 [th] .

4.3 Distributions for Good and Raining PMTs

The histograms of the values of the VEM Peak, the Dynode/Anode Ratio as well as the RMS and the Maximum-Minimum of them are discussed in the next chapters.

4.3.1 Distributions of the VEM Peak and Dynode/Anode Ratio

Following the method of the analysis, firstly the distributions of the VEM   Peak and Dynode/Anode Ratio for good and raining PMTs are analysed. They are shown in Figure 4.3.
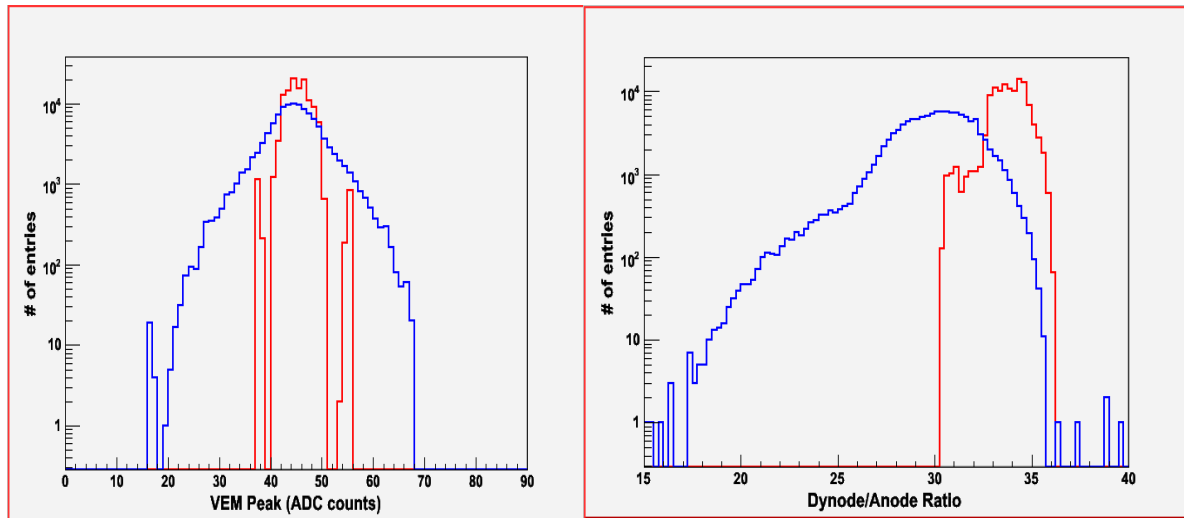
Figure 4.3: Distributions for VEM Peak and Dynode Anode Ratio (good PMTs: red color, raining PMTs: blue color).

We can conclude that for good PMTs the distibutions are narrow but for raining PMTs the distributions are much more spread. The number of entries in each histogram is around 120000.

For the VEM Peak distributions, both good and raining PMTs have approximately the same mean value, while the spread of values is much larger for the raining PMTs.

For the Dynode/Anode Ration also the mean value is different for raining and good PMTs. The spread of the distribution is much larger for the raining PMTs.

4.3.2 Distributions of the RMS and MAX-MIN for the VEM Peak

For the fact, that raining PMTs produce fluctuations of the value of the VEM Peak, we analyse the distributions of the RMS and the MAX-MIN of it. In Figure 4.4, the distributions for good and raining PMTs are presented.
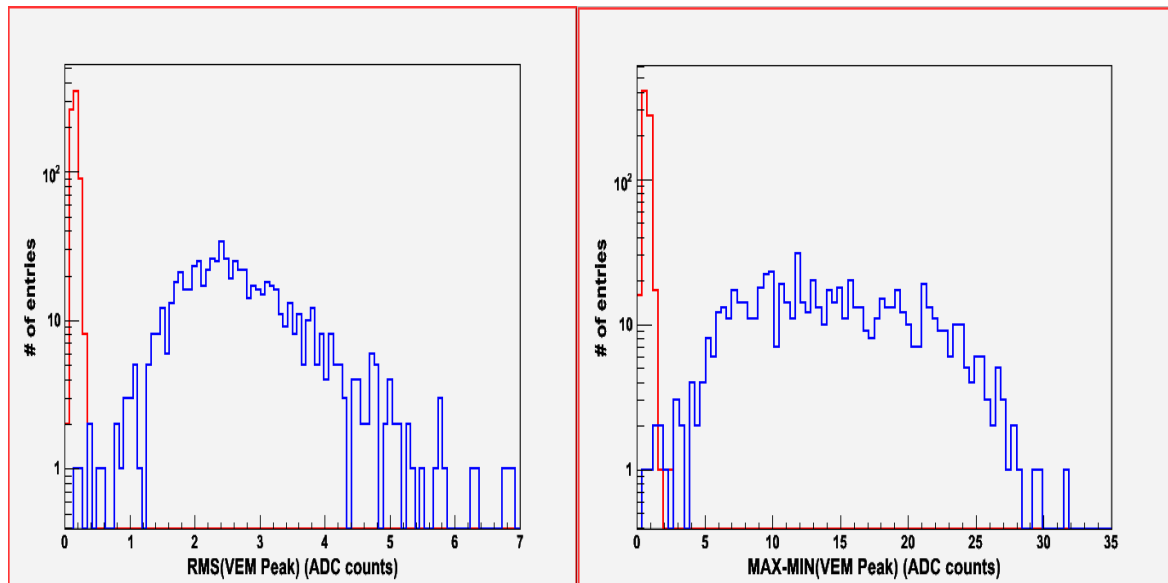
Figure 4.4: Distributions of the RMS and MAX-MIN for the VEM Peak (good PMTs: red color, raining PMTs: blue color).

Both for the RMS and the MAX-MIN histograms, the distributions for good and raining PMTs look completely different. While the good PMTs have a very narrow distribution with also a small mean value, the raining PMTs show a wide distribution with a much larger mean value. There is basically no overlap between the two distribution. The number of entries in each histogram is around 700.

4.3.3 Distributions of the RMS and MAX-MIN for the Dynode/Anode Ratio

The other parameter in our analysis is the Dynode/Anode Ratio. The distributions of the RMS and MAX-MIN of the Dynde/Anode Ratio for good and raining PMTs are shown in Figure 4.5.
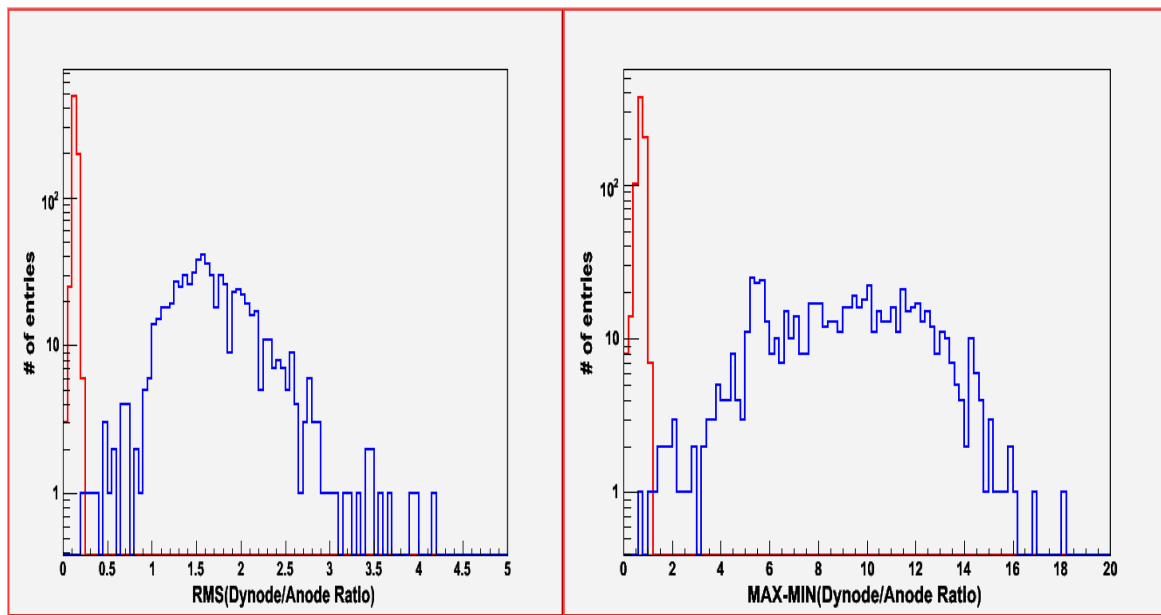
Figure 4.5: Distributions of the RMS and MAX-MIN for the Dynode/Anode Ratio (good PMTs: red color, raining PMTs: blue color).

The distributions of the RMS and the MAX-MIN for good and raining PMTs are totally different. Therefore, we can observe that also for the Dynode/Anode Ratio, the distributions of the good PMTs are very narrow with mean value close to zero, but for raining PMTs this value is much larger with a spread distributions. The number of entries in each histogram is around 700.

4.4 Correlation Plots for Good and Raining PMTs

The correlation plots between the Dynode/Anode Ratio and the VEM Peak of the selected 100 good and 100 raining PMTs are presented in Figure 4.6.
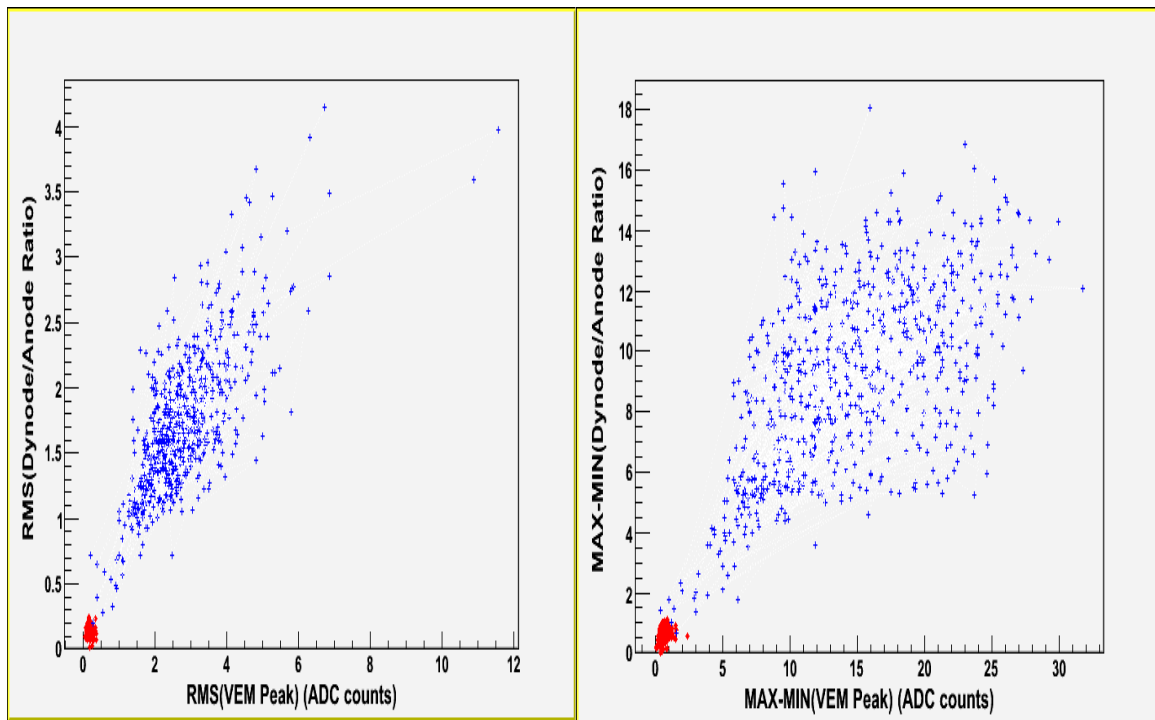
Figure 4.6: Correlation plots between the Dynode/Anode Ratio and the VEM Peak (good PMTs: red color, raining PMTs: blue color).

It is possible to observe in both plots tht the raining and the good PMTs are clearly separated. In both correlation plots the same pattern is identified for good and raining PMTs. The RMS plot shows a more evident separation, therefore the RMS is sufficient in order to select the raining PMTs.

Figure 4.7 shows the other correlation plots for the other combinations of those variables.
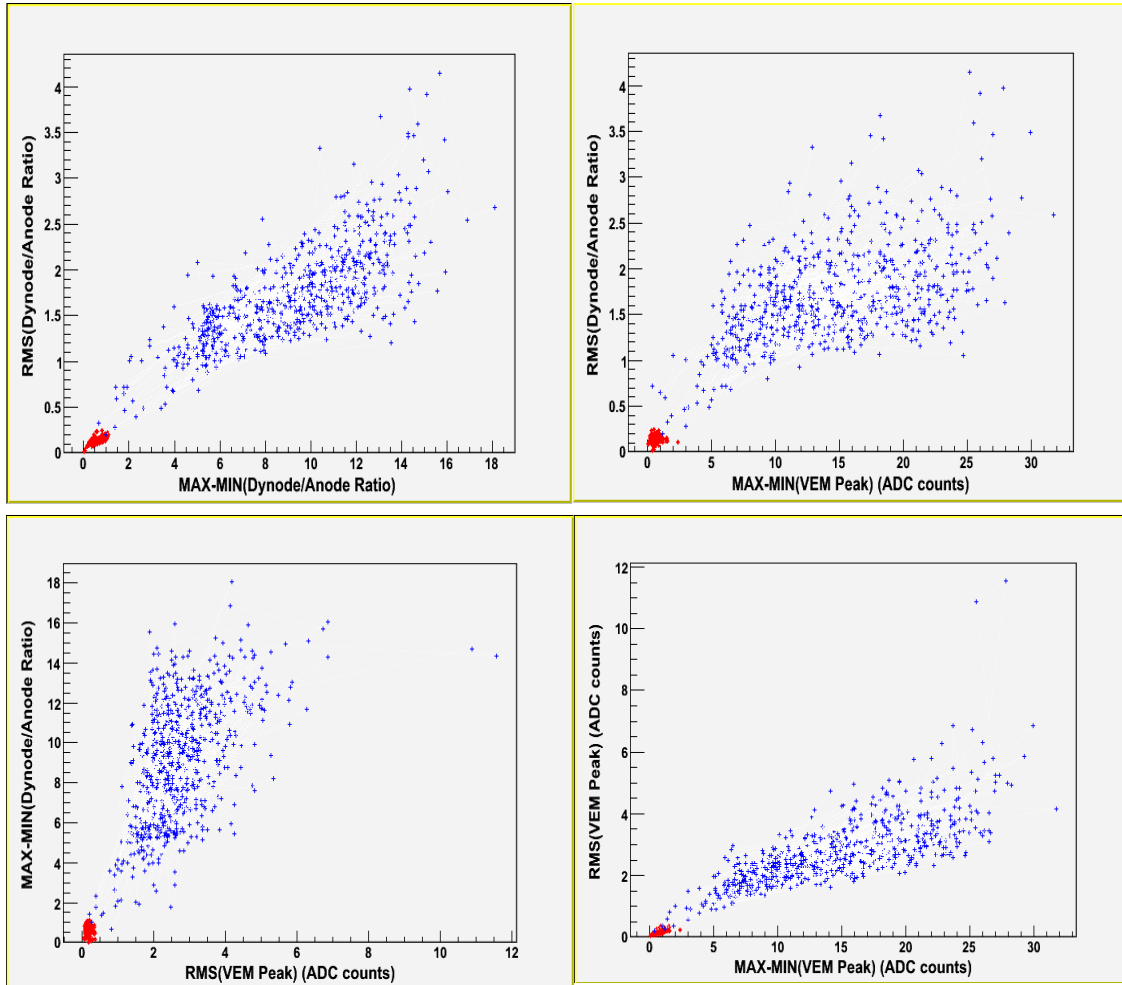
Figure 4.7: Correlation plots between the Dynode/Anode Ratio and the VEM Peak (left top:RMS(Dynode/Anode Ratio versus MAX-MIN(Dynode/Anode Ratio), right top: RMS(Dynode/Anode Ratio) versus MAX-MIN(VEM Peak), left bottom: MAX-MIN(Dynode/Anode Ratio) versus RMS(VEM Peak), right bottom: RMS(VEM Peak) versus MAX-MIN(VEM Peak).

In Figure 4.7, we can see that all plots have the good and raining PMTS very clearly separated as in Figure 4.6. They show the same pattern of the figure 4.6. So, it is sufficient to use two variables in order to select the raining PMTs. We choose the RMS of the VEM Peak and the RMS of the Dynode/Anode Ratio in order to separate them.

4.5 Thresholds

In order to separate the good PMTs from the raining PMTs, first we proceed to do a gaussian fit to the distribution of the RMS for good PMTs. Figure 4.8 shows the gaussian fits of them.
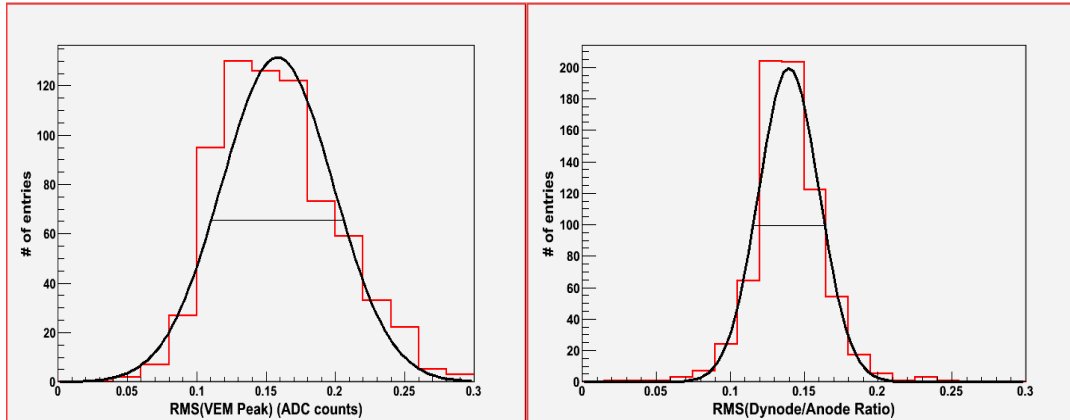
Figure 4.8: Gaussian fits to the distributions of the RMS for good PMTs.

For the distribution of the RMS of the VEM Peak, the gaussian fit has a mean value of around 0.158 ±0.002 ADC counts with a standard deviation of 0.040±0.001 ADC counts. So, the width of this gaussian is about 0.094±0.002 ADC counts.

The gaussian fit for the Dynode/Anode Ratio has a mean value of 0.140±0.001 with a standard deviation of 0.020±0.001, Therefore the Full width at half maximum is approximately 0.047±0.002 ADC counts.

Thus, we proceed to do a gaussian fit to the distributions of the RMS for good and Raining PMTs. Figure 4.9 shows the gaussian fits.
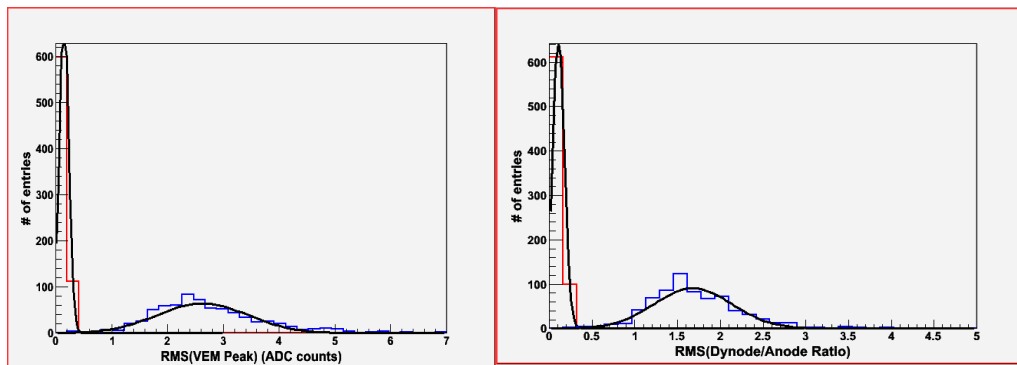
Figure 4.9: Gaussian fits to the distributions of the RMS for good and raining PMTs.

The aim of this study is identify raining PMTs. This information can then be used to repair these PMTs or to treat them differently from good PMTs in certain analyses. For this purpose the value where the gaussian fits for the good and raining PMTs intercept has been chosen. The values are 0.5 ADC counts for the RMS of the VEM Peak and 0.5 ADC counts for the RMS of the Dynode/Anode Ratio. Both values are much more than 5 standard variatons away from the mean of the distribution of the good PMTs. This ensures that only a very small number of good PMTs is wrongly identified as a raining PMT.

4.6 Dependence of the Raining Behaviour on the Station Id

This raining behaviour appeared for the first time for stations installed after January 2005. Most of the stations with raining PMTs have therfore Id>600. It is possible to observe this carachteristic in Figure 4.10 for the RMS of the Dynode/Anode Ratio versus the Id of the local station.
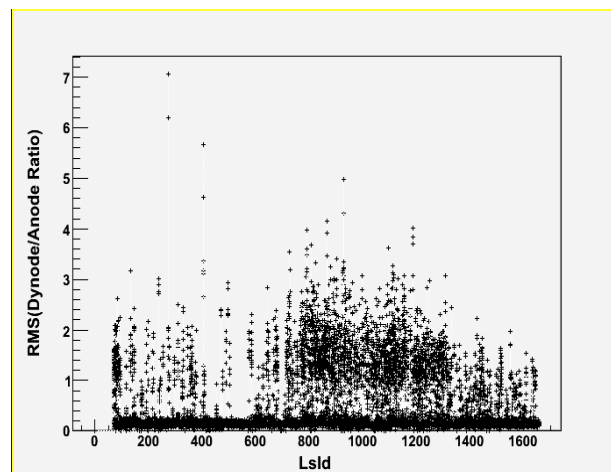
Figure 4.10: Plot of the RMS (Dynode/Anode Ratio) versus the Id of the local stations for all the PMTs.

Many of the PMTs for the stations with Id more than 600 have high values of the RMS, so many PMTs with Id>600 are affected by this instability.

For other hand, a test on a tank with 2 raining and 1 good PMTs was made with the standard electronics and power system excluded. Another power sytem was used and the response of the 3 PMTs to the LED light was studied by a oscilloscope. The result was that the instability is independent on the characteristic of the local station or on the electronics/power systems [29].

4.7 Dependence of the Raining Behaviour on the Temperature

The PMT instability appears to be caused by temperature variations. Thus, it is important to consider the variation of the temperature in the analysis. The plot of the VEM Peak (left side) versus time and the plot of the average temperature versus time during 6 months are shown in Figures 4.11 The data are obtained every hour from the Long Term Monit Calib Table.
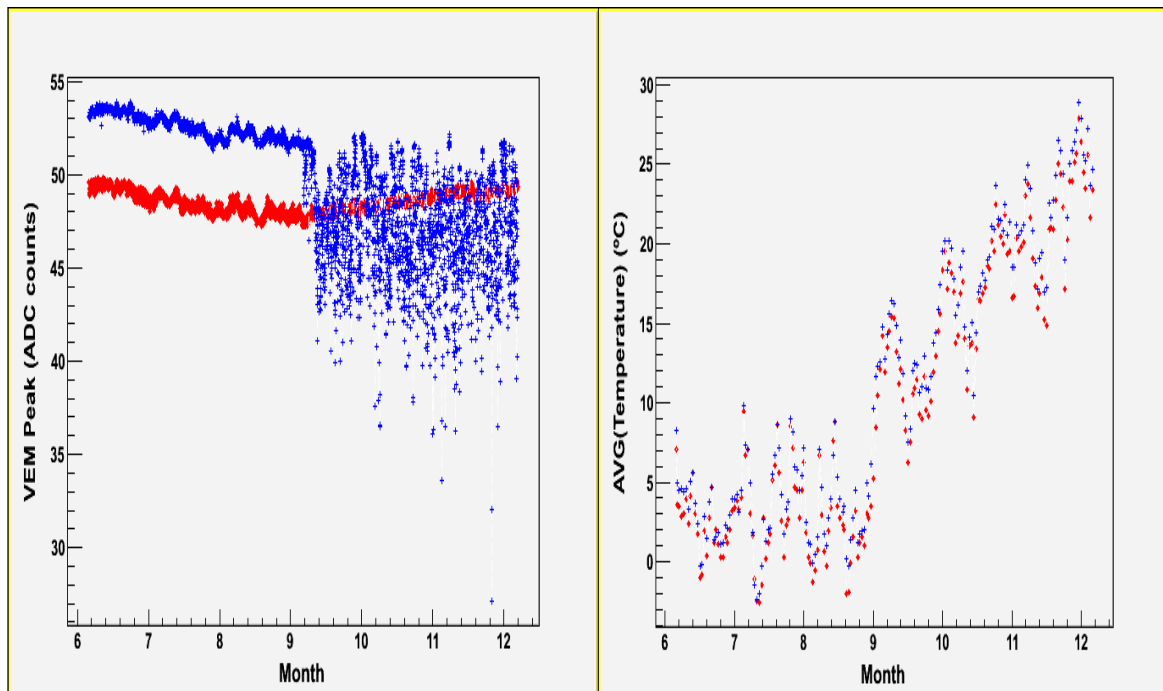
Figure 4.11: Plot of the VEM Peak and the Average (Temperature) versus time (Good PMT, red color: LsId=113 PMT2; Raining PMT, blue color: LsId=308 PMT1).

In the plot it is possible to observe that the variation of the temperature does not affect the good PMT .   But the raining PMT seems to work properly up to September (low temperatures).

The variable of the raining PMTs, the Dynode/Anode Ratio also is affected in the same characteristic. Figure 4.12 shows the same behaviour of this temperature dependence.
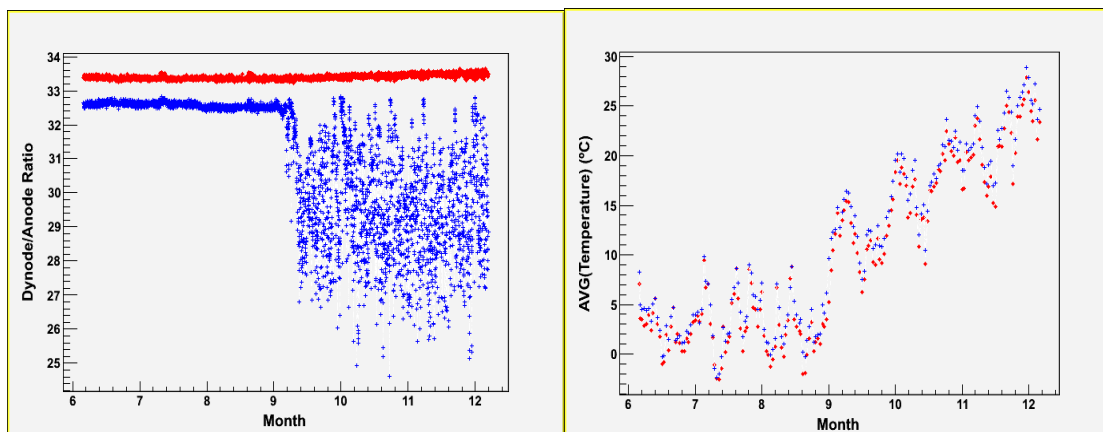
Figure 4.12: Plot of the Dynode/Anode Ratio and the Average (Temperature) versus time (Good PMT, red color: LsId=113 PMT2; Raining PMT, blue color: LsId=308 PMT1).

The raining effect appears when the temperature is high (September to December in Malargue, Argentina). The plots for the other raining PMTs show the same pattern with respect to the temperature. Thus, raining behaviour is an effect dependent on the temperature and there is a dependence between the raining effect and higher temperatures. During the warm season the number of raining PMTs is around twice as large as in the cold season. [29].

4.8 Dependence of the Raining Behaviour on the High Voltage

For the same raining and good PMT of the last chapter, the plot of the high voltage as a function of time is presented in Figure 4.13 during the same period of time, in order to see if there is a correlation between the raining effect and the High Voltage.
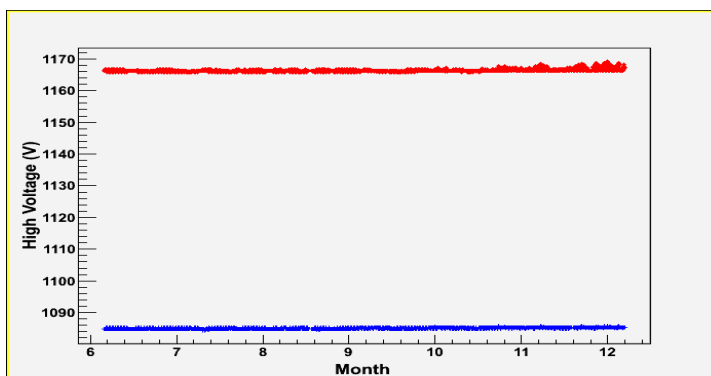
Figure 4.13: Plot of the High Voltage of the PMT versus time (Good PMT, red color: LsId=113 PMT2; Raining PMT, blue color: LsId=308 PMT1).

It is possible to observe that both for the good and raining PMT the high voltage is stable for the whole long period of time. The other plots for the other raining PMTs show the same behaviour with respect to the High Voltage variable, showing that there is no dependence of the raining effect on the High Voltage of the PMT.

Chapter 5

Another bad behaviour of the PMTs: High PMT gain changes

5.1 Correlation plots for all PMTs

In the previous chapter the behaviour of raining PMTs has been studied. It has been shown that for a preselected sample of PMTs there is a strong correlation between the RMS of the Dynode/Anode Ratio and the RMS of the VEM Peak. As a next step these variables are studied for all PMTs. A correlation plot between the RMS of the Dynode/Anode Ratio and the RMS of the VEM Peak for all PMTs is presented in Figure 5.1.
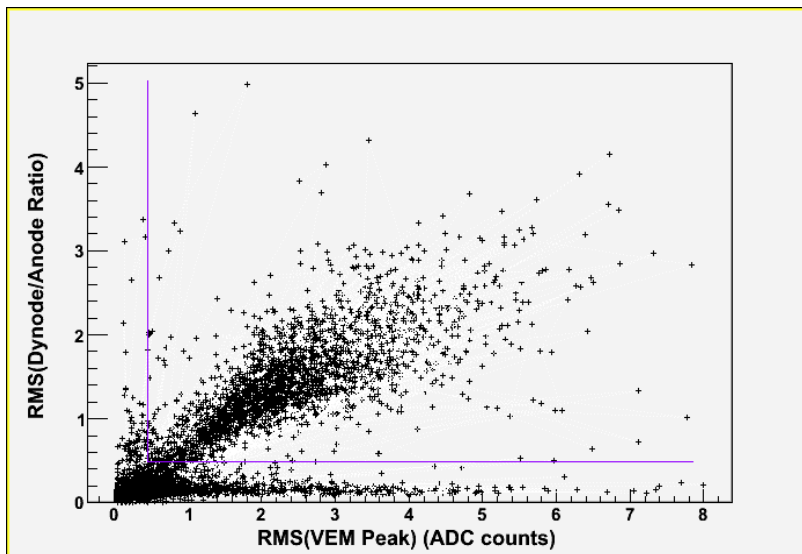
Figure 5.1: Correlation plots between the Dynode/Anode Ratio and the VEM Peak for all PMTs.

In Figure 5.1, it is possible to observe a strong correlations for many events. They are the raining PMTs. In order to separated the raining PMTs from the others, a cut based on the distributions of the RMS of the VEM peak   (Figure 4.4) and of the RMS of the Dynode/Anode Ratio (Figure 4.5), is applied. A clear separation of the raining PMTs from the other PMTs is observed.

Other clear group of PMTs with large values only for the RMS of the VEM Peak and with the RMS of the Dynode/Anode Ratio approximately less than 0.5 is observed. This type of PMT is the objective of the analysis of this chapter.

5.2 Distributions and Thresholds.

The distributions of the RMS and the MAX-MIN of the VEM Peak are shown in Figure 5.2.
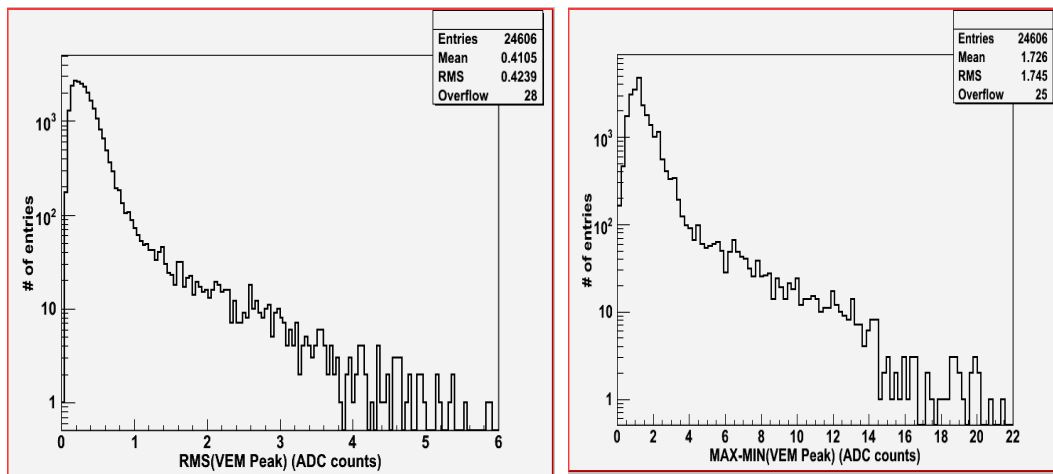
Figure 5.2: Distributions of the RMS and MAX-MIN for the VEM Peak

There is a strong maximum of PMTs with a low value and a very long tail of PMTs with much larger values. The same pattern is obseved in both distributions.

Besides, the correlation plots between the RMS and the MAX-MIN of the VEM Peak are presented in the figure 5.3.   It is possible to observe in the figure strong correlation between the RMS and the MAX-MIN of the VEM Peak. So, RMS is sufficient in order to select these PMTs.
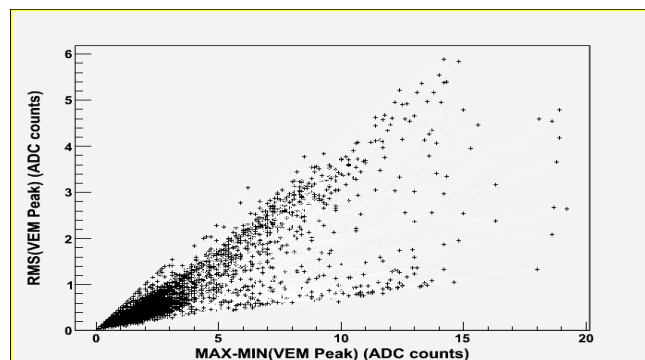
Figure 5.3: Correlation plots between the RMS and the MAX-MIN of the VEM Peak

In order to obtain the value where we have to separate this bad behaviour of photomultiplier from the good PMTs, we use the Full width at half maximum of the distribution. It has the value of 0.4 ADC counts. We assume that the distribution consist of two parts: one gaussian distribution for the good PMTs and a tail stemming from PMTs with abnormal behaviour. Therefore one can approximate the standard deviation of the gaussian part from the FWHM of the distribution. The standard deviation has the value of 0.15 ADC counts. In order to be sure that the good PMTs do not mix with the bad PMTs, we choose 5 standard variation away from the mean of the distribution. Thus, the value is 1 ADC count for the RMS of the VEM Peak.

5.3 Example of the Behaviour for those PMTs.

An example of a bad PMT (green color) compared to a normal PMT (red color) is shown in the figure 5.4.
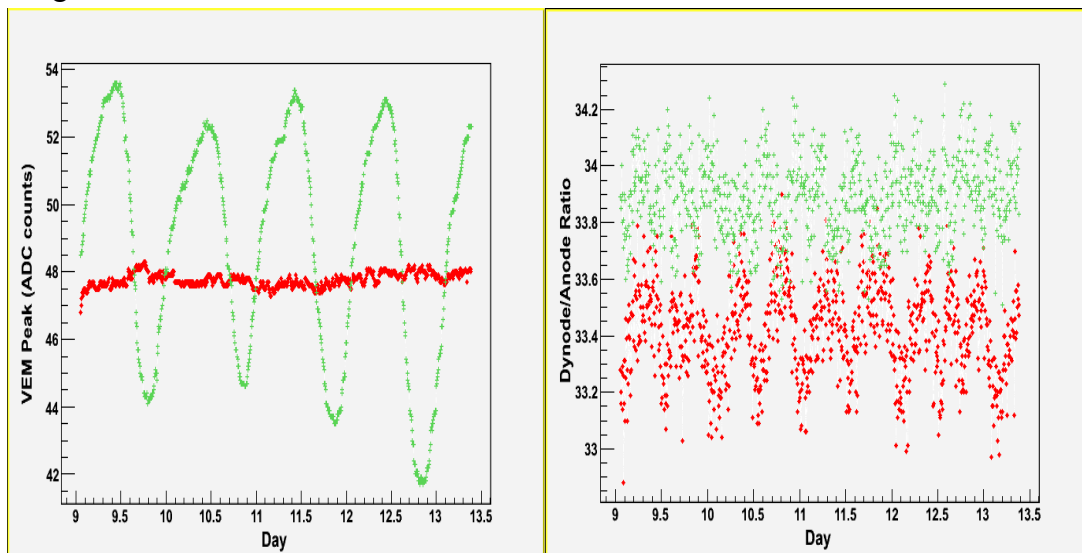
Figure 5.4: Plot of the VEM Peak and Dynode/Anode Ratio versus time (Good PMT, red color: LsId=117 PMT3; Bad PMT, green color: LsId=1431 PMT2).

The pattern of daily variations for good PMTs are very small whereas but for the bad PMTs large variations of sinoidal form of often more than 10 ADC counts for the VEM Peak occur. If we compare this plot with the figure 3.1, we observe that there is a strong linear correlation with the temperature. In addition there are not sudden jumps, so no problem for data taking.

5.4 Dependence of the Behaviour for the VEM Peak value on the Temperature

This bad behaviour of those PMT appears to be caused due to temperature variations. Thus, it is important to consider the variable of the temperature in the analysis. The plot of the VEM Peak (left side) versus time and the plot of the average temperature versus time for the same PMTs (last chapter) during 6 months are shown in the figures 5.5. The data are obtained every hour from the Long Term Monit Calib Table.
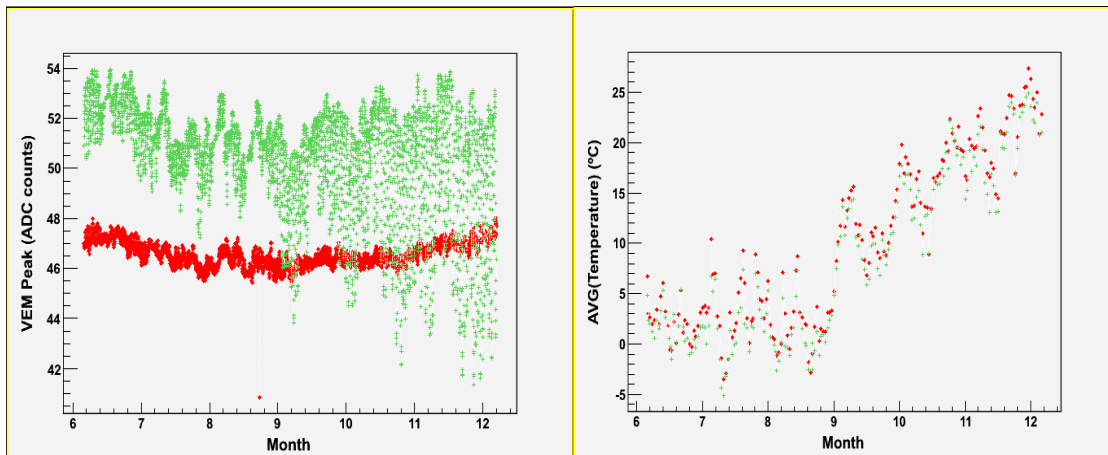
Figure 5.5: Plot of the VEM Peak and the Average (Temperature) versus time.

In the plot, it is possible to observe that the variation of the temperature does not affect the good PMTs. But the bad PMT behaviour is more intense when the temperature is high (September to December in Malargue, Argentina).

The plots for the other bad PMTs show the same pattern with respect to the temperature. Thus, this bad behaviour is an effect dependent on the temperature and mainly there is a dependence with the higher temperatures. It is supposed that the problem is related with the base of the PMT (by temperature effects) or with the life cycle of the PMT [28].

5.5 Dependence of the Behaviour for the VEM Peak on the High Voltage.

The plot of the high voltage versus time is presented in the figure 5.6 for the same bad PMT during the same period of time, in order to see if they are affected for the High Voltage variable.
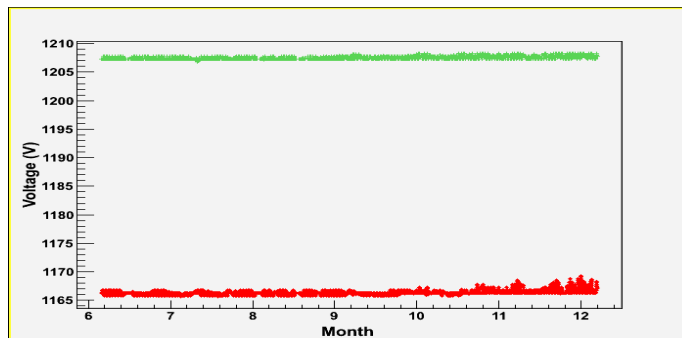
Figure 5.6: Plot of the High Voltage of the PMT versus time.

It is possible to observe that for the bad PMT the high voltage is stable for the long period of time. The other plots for the other bad PMTs show the same behaviour with respect to the High Voltage variable, showing that there is not dependence of the this carachteristic on the high voltage of the PMT.

Chapter 6

Alarms Creation

6.1 Introduction.

The aim of the monitoring data is to find problems with the data taking as soon as possible. The optimal way is to identify problems before they diminish the quality of the data. In the near future several classes of alarms have to be created, from those which might cause problems to those which need immediate action by one of the shifter. Therefore, after that the analysis of the respective parameters of the problem is done, it is necessary to define the respective alarm for them.

6.2 Language Programming.

For the creation of the Monitoring Alarm, the following language programmings are used :

- We use C++ compiled language. It has the advantages: availability, portability, speed, generality, reusability and object orientation. Object oriented programming is a strategy for simplifying the programming task.

- MySQL database management system. It is needed in order to add, access, and process data stored in a computer database.

- ROOT: an object-oriented framework. It is aimed to solve the data analysis challenges of high-energy physics. In this framework the basics services like graphics and histograms are provided.

The alarm code should be written in an efficient way. So, it is recommended to have an elaborate and efficient MySQL request in order to have a fast MySQL request and to reduce the C++ code. Thus, it is necessary to use the large panel of options offered by MySQL. In general, the condition of the alarm should be in the request itself.

6.3 Free Disk Alarm.

In this chapter the procedure of the alarm creation is described with the example of the Free Disk alarm. This alarm was created within the scope of this thesis and is already installed in the Auger Online Monitoring . The disk of each local station is a RAM disk with a capacity of 2 Mega Bytes [30].

Figure 6.1 shows one example of the behaviour of the Free Disk space for one local station as a function of time.
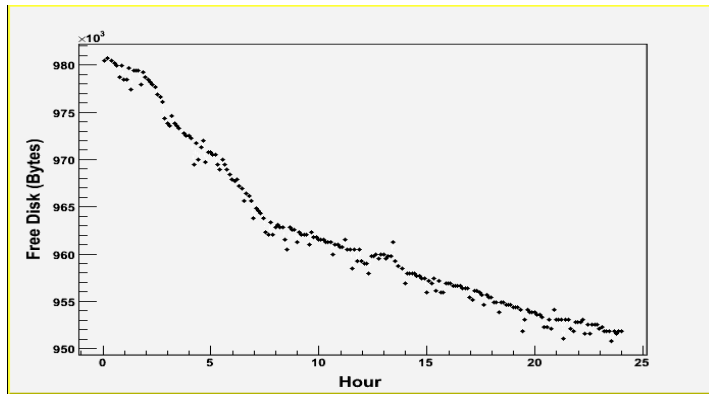
Figure 6.1: Plot of the Free Disk versus time (LsId: 1200, date: 10.12.2007)

As too little space can create problems in data taking, stations with values of the Free Disk below a given threshold should trigger a alarm. Figure 6.2 shows the distribution of the Free Disk variable for 8 days (6-13) in December 2007 for all the local stations.
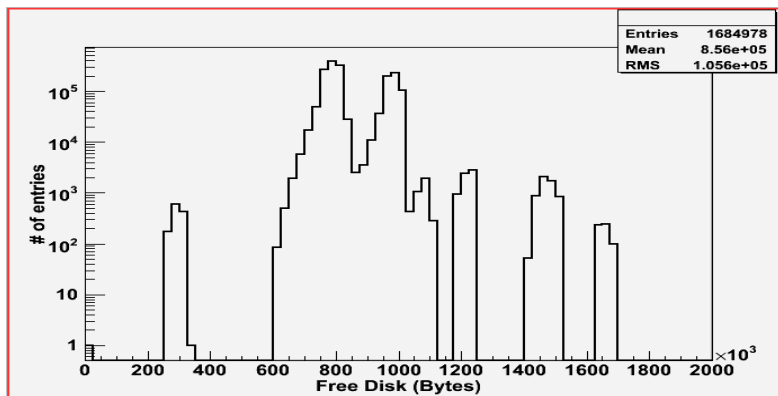
Figure 6.2: Distribution of the Free Disk for all local stations.

54

From the distribution, it is possible to observe that nearly all stations have values of the Free Disk of more than 600000 Bytes. This value corresponds to the chosen threshold. The algorithm of the alarm is:

If for one local station the Free Disk<600000 Bytes (30 %) the alarm is triggered.

If the alarm is triggered, shifter action should be to report to the Surface Detector Team that there is a local station with too low free disk space.

6.4 Raining and High PMT gain change alarms.

The procedure of the alarms for raining and high PMT gain change can be realized in the same way that the Free Disk Alarm was done in the last chapter. The only differences are the conditions for the alarm, the selected variables and the threshold values.

The RMS of the VEM Peak and Dynode/Anode Ratio are the variables chosen for the alarms (chapter 4.5 and 5.2). The conditions an the thresholds values are:

- From the analysis of the raining PMTs (chapter 4), a threshold of:

    RMS(VEM Peak)>0.5 ADC counts and RMS(Dynode/Anode Ratio)>0.5
    should be used for the raining alarm.

- In the chapter 5 the analysis of the another bad behaviour (high PMT gain change) of the PMTs was done and so, a threshold of:

    RMS(VEM Peak)>1 ADC count and RMS(Dynode/Anode Ratio)<0.5
    should be used in order to select those PMTs.

6.5 Wiki information.

For each alarm a wiki entry is created. The wiki information should contain all the information about the alarm, the threshold values, the algorith of the alarm, plots, histograms, physical informations,..etc.

Also it is necessary to specify which shifter action has to be performed if the alarm is triggered. Further information as the bibliography and contribute notes where it is possible to find more information concerns to the alarm is necessary to document.

Chapter 7

Summary and Conclusions.

The principal objective of this thesis was to present the monitoring and analysis of the data taking of the Pierre Auger Observatory (PAO), specially of the photomultipliers of the Surface Detector. The results of this analysis show that there are PMTs with bad behaviour, mainly with high fluctuations of the VEM Peak and/or the Dynode/Anode Ratio. They are called in our analysis Raining PMTs and High Changes PMT Gain.

Raining PMTs show sudden fluctuations (reason of the "raining" name) of the VEM Peak and the Dynode/Anode Ratio. They show a strong correlation between RMS(VEM Peak) and RMS(Dynode/Anode Ratio). In order to select raining PMTs, a cut of RMS(VEM Peak)>0.5 ADC counts and RMS(Dynode/Anode Ratio)>0.5 should be used. It has been observed that the raining behaviour depends on the temperature and it appears especially when the temperature is high.

Raining PMTs have been tested in Grenoble (France) and a repair solution was found and all PMTs will be repaired in the near future. On the other hand, Raining PMTs affects the calibration of the detector (increased of the ToT trigger rate), but they do not affect the energy reconstruction for events with E>10^{19} eV.

Another bad behaviour of PMTs (high PMT gain change) with large values only for the RMS of the VEM Peak and with the RMS of the Dynode/Anode Ratio approximately less than 0.5 is observed. This type of PMT we call High Changes PMT Gain. This bad behaviour also is an effect dependent on the temperature and mainly there is a dependence with the higher temperatures. In order to select those PMTs a cut of RMS(VEM Peak)>1 ADC count and RMS(Dynode/Anode Ratio)<0.5 ADC counts should be used.

At the end, the purpose of the monitoring data is to find problems with the data taking as soon as possible and in this form to do the respective alarm for them. Shifter actions have to be performed if the alarm is triggered. For the alarm creation procedure, firstly the analysis in order to find the threshold values for the parameters of the alarms should be done. It was the objective of the chapter 4 and 5 for the raining and High Changes PMT Gain respecively.

The Free Disk alarm also was presented and this alarm is already installed in Auger Online Monitoring. This alarm is triggered when the disk of one local station has low capacity (less than 600000 Bytes).

Finally, it is important to implement new alarms as soon as the experts report new future problem in the detectors.

List of Figures

List of Formulas

List of Acronyms

PAO: Pierre Auger Observatory

PMTs: Photomultipliers

SD: Surface Detector

GZK: Greisen-Zatsepin-Kuzmin

EAS: Extensive Air Shower

UHECR: Ultra High Energy Cosmic Rays

AGASA: Akeno Giant Air Shower

CMB: Cosmic Microwave Background

CDAS: Central Data Acquisition System

GPS: Global Positioning System

FD: Fluorescence Detector

ADC: Analogic Digital Converter

FADC: Fast/Flash Analog Digital Converter

VEM: Vertical Equivalent Muon

Q^{peak}_{VEM} :   Peak in a charge histogram

I^{peak}_{VEM} :   Peak in a pulse height histogram

ToT: Time over Threshold

LS: Local Station

MonitCalib: Monitoring Calibration

LongTermMonitCalib: Long Term Monitoring Calibration

RMS: Root Mean Square

MAX-MIN: Maximu minus Minimum

LsId: Id of the Local Station

RAM   Random Access Memory

List of Tables

Bibliography

[1] Emilio Segré, Nuclei and Particles, The Benjamin/Cummings Publishing Company, Inc. 1977.

[2] M. T. Dova (Pierre Auger Collaboration), Survey of the Pierre Auger Observatory, Proc. ICRC 2001.

[3] Donald Perkins, Particle Astrophysics, Oxford University Press, 2003.

[4] C. Grupen, Astroparticle Physics, Springer-Verlag Berlin Heidelberg, 2005.

[5] M. Lemoine, Physics and Astrophysics of Ultra-High Energy Cosmic Rays, Springer-Verlag Berlin Heidelberg 2001.

[6] R.W. Clay, A . G. K. Smith and J. L. Reid, Cosmic Ray Induced Noise in Gravitation Wave Detectors, Electronic Publications of the Astronomical Society of Australia, Vol. 14, Number 2.

[7] Pierre Auger in Collaboration with P. Ehrenfest, R. Maze, J. Daudin, Robley, A. Freon, Extensive Cosmic-Ray Showers, Rev. of Modern Physics, Vol. 11, 288-291 (1939).

[8] Symmetry, volume02, issue01, February 05.

[9] Bluemer, J. (Pierre Auger Collaboration), Status and Perspectives of the Pierre Auger Observatory,   Proc. the 28th International Cosmic Ray Conference.

[10] Iona Dutan, Laurentiu Caramete, Alex Curutiu, Iona C. Maris, Ona Tascau, Peter L. Biermann, The origin of Ultra high energy cosmic rays: A complete sample of predicte sources and a predicted sky distribution of events (UHECR-X), GAP Note 2007-109.

[11] Todor Stanev, Ultra-High-Energy Cosmic Rays and the Large-Scale Structure of the Galactic Magnetic Field, Astrophysical Journal 479, Report Number BRI-96-32, 1997.

[12] Oliver Deligny, Antoine Letessier-Selvon, Etienne Parizot, Magnetic horizons of UHECR sources and the GZK feature, Elsevier Science, 2007.

[13] Pierre Auger Collaboration, The Pierre Auger Observatory Design Report, Second Edition, 1997.

[14] Nishant Mehta, Helio Takai, Simulation and Detection of Extensive Air Showers, Brookhaven National Laboratory, 2003.

[15] Ronald Cintra Shellard (Pierre Auger Collaboration), First Results from the Pierre Auger Observatory, Brazilian Journal of Physics, Vol. 36, No.4, 2006.

[16] M. Kleifges and H. Gemmeke (IEEE for the Auger Collaboration), UHE Cosmic Ray Detection with the Pierre Auger Observatory, IEEE Transactions on Nuclear Science , Vol. 51, Issue 3, Part 1, 2004.

[17] Enrique Zas, ZeV Air Showers: The View from Auger, Article from Physics Department, University of Santiago of Compostela.

[18] B. Genolini, L. Raux, C. de La Taille, J. Pouthas, V. Tocut, A Large Dynamic Range Integrated Front-End for Photomultiplier Tubes, Beaune ,2005, Poster I-8.

[19] D. Nitz (Pierre Auger Collaboration), The Front-End Electronics for the Pierre Auger Observatory Surface Array, IEEE Vol.51, No.3, 2004.

[20] X. Bertou, P. S. Allison, C. Bonifazi, P. Bauleo (Pierre Auger Collaboration), Calibration of the Surface Array of the Pierre Auger Observatory,GAP note: 06-012.

[21] A. tripathi, X. Bertou, A. Chou, A sistematic calibration of Surface Detectors using Muon Data from the Engineering Array, GAP note 2002-046.

[22] M.A. L. de Oliveira, Pierre Auger Observatory: status report, Brazilian Journal of Physics, Vol. 34, No. 4a, 2004.

[23] Xavier Bertou (Pierre Auger Collaboration), Calibration of the surface array of the Pierre Auger Observatory, Proc. of 29th International Cosmic Ray Conference Pune, 2005.

[24] Johannes Bluemer (Pierre Auger Collaboration), Status and Perspectives of the Pierre Auger Observatory, Acta Physica Polonica B, No 6-7, Vol. 35, 2004

[25] D. Allard, E. Armengaud, I. Allekotte, The trigger system of the Pierre Auger Surface Detector: operation, efficiency and stability, Proc. of 29th International Cosmic Ray Conference Pune, 2005.

[26] Cyril Lachaud (Pierre Auger Collaboration), Pierre Auger Observatory: Overview of the Acquisition Systems, LPCC/CDF, Paris, France.

[27] R. Meyhandan, J. Matthews, D. F. Nitz, Auger front-end ASIC simulations, Proc. ICRC 2001: 777, GAP note: 2001-039.

[28] Paul Lebrun, On the Fluctuating PMT gain, SD Monitoring Analysis, GAP Note-2007-042.

[29] W. Fulgione, About raining PMTs, GAP Note-2007-081.

[30] P. Frenkel, JM. Brunet, L. Guglielmi, G. Tristan, Evaluation of the Central Station Hardware, France, 1997, GAP note: 1997-041

[31] Auger Collaboration, Properties and performance of the prototype instrument for the Pierre Auger Observatory, Nuclear Instruments & Methods in Physics Research A 523, 2004.

Acknowledgements